# SSNTD Technique in Photo-neutron Applications

Laszlo Sajo-Bohus[1,a*] and Hector Rene Vega-Carrillo[2,b]

[1]Universidad Simón Bolívar, Nuclear Physics Laboratory, Apdo 89000, Caracas 1080A, Venezuela

[2]Universidad Autónoma de Zacatecas, Unidad Académica de Estudios Nucleares, C. Ciprés 10, Fracc. La Peñuela, 98068 Zactecas, Zac. México

[a]sajobohus@gmail.com (*corresponding author), [b]fermineutron@yahoo.com

**Keywords:** Passive Detectors. Photo-neutrons. Radiotherapy, SSNTDs, Linac.

**Abstract.** Passive Solid State Nuclear Track Detectors (SSNTDs) are a versatile tool for neutron studies as has been shown long ago and several good quality materials are commercially available. They are useful for charged particle detection in the linear energy transfer (LET) range above the threshold value of ~10 keV $\mu m^{-1}$. Linacs, operating above 6 MeV up to the energy region where radiotherapy is applied usually up to ~25MeV, induce unwanted photo-neutron field; their spectra shows two components due to reaction dynamics based on evaporation and knock-on mechanisms. Neutrons produced by Linacs are often neglected in health application; however, today it has become necessary to assess the effect on patient, staff and radiation workers. Radiation studies using SSNTDs play a major role in this case. Other fields also take advantage of the passive detectors properties; in fact they are employed with success to measure neutron signals relevant for plasma diagnostics as it was demonstrated at the RFX facility as part of the ITER project. The PADC-NTD techniques provide information on external neutron field values around the RFX-installation during pulsed operation. In any case, converter materials, as charged particles from (n, p) and (n, $\alpha$) reactions, are required to produce neutron fingerprints through latent tracks. These once etched provide information on neutron fluence spatial values. Track histograms are then employed to determine photo-neutron induced damage in materials as well as radiation dose to both patient and professionally exposed workers. The estimated neutron fluence that can be determined by NTM covers a large range of values, the largest being above $10^{10}$ (± 12%) neutrons/$cm^2$.

## Contents of Paper

## 1. Introduction

Neutrons as tool have been extensively employed for nuclear transmutation, to determine the elemental composition [1, 2], and the structure of materials. Also, neutrons have been used to evaluate the performance of systems and materials in different environments like space, for dosimetric purposes [3], plasma physics and fusion reactions [4, 5]. Furthermore, they are used for the detection and localization of explosives, even in well shielded packages, among others [6-8].

Lesser known are neutron techniques for demining programs [9], illicit material detection [11, 12] or neutron holography [13, 14]. In basic and interdisciplinary science, neutrons have been recognized as an important component. Regardless of their applications, several features about the neutron production mechanism or energy spectra need to be determined, and Nuclear Track Methodology (NTM) often is preferred.

During the past years an increasingly large number of accelerator-based facilities entered in operation in radiotherapy and industrial applications. Linear accelerators (Linacs) produce high energy electrons that are used for cancer treatment, sterilization of medical devices and materials, non-intrusive inspection of cargo containers, etc. Also, electrons are used to induce energetic *bremsstrahlung* photons for cancer treatment [15, 16]. The photo-nuclear interaction between bremsstrahlung photons and the nuclei produces neutrons (named photo-neutrons) [17, 18].

The photon interacts with nuclei through three processes: Giant dipole resonance, Quasi-deuteron effect and Photo-pion decay. These take place and neutron contamination in radiotherapy halls and industrial facilities occurrs; as a consequence, a radiation protection issue is at hand because of delivery of a nondesirable dose to patients and humans alike. The neutron interaction with materials inside the hall induces neutron activation that contributes to the absorbed dose for the facility staff. In order to improve the radiation protection protocols, and to estimate the risk for the patient and workers, it is important to opt for the neutron characterisation [19, 20].

## 2. Basic Fundamentals of Neutron Detection by SSNTDs

Several physical phenomena have been studied in relation to energetic photon producing neutrons when absorbed by matter. Photons interacting with the atomic nucleus, produce photo-neutrons and their occurrence depends on the incident energy above the neutron binding energy; the mentioned nuclear process is explained by Giant Dipole Resonance (GDR) interaction mechanism [18].

For a given energy window, neutral particles are produced by photonuclear ($\gamma$, n) and ($\gamma$, 2n), electronuclear (e, e'n), and ($\gamma$, p) reactions [15-19]. In the case photons impinging on heavy targets, e.g. U, or Th, then also fission takes place, in this case neutrons are produced as a consequence of photon absorption or photo-fission-neutron; on average neutron production is 2.5 neutrons per fission. Independently of the reaction mechanism, once it is produced, neutrons undergo elastic collisions with hydrogen rich matter or components of concrete walls, ceiling and floor of the facility.

In NTM, neutrons are detected by SSNTDs following an indirect process in which neutrons are converted in the detecting materials as charged particle by scattering or (n, x) nuclear reaction. To register these and other nuclear events by NTM, usually two conditions should be met, i.e. a charged particle must accompany it and at the same time, have energy above the threshold value (200 keV). A set of detecting matter, SSNTD-type, meet the physical conditions to provide a proper fingerprint (a latent track), so that the neutron related incident ion should have the possibility to penetrate the detecting matter with a length of several hundred nanometres. In the case of polycarbonate that length corresponds to about one thousand monolayers. Once a large number of

atoms become ionized, then electronic recombination takes over and at its completion a latent track materializes; during this process the Coulomb explosion alters molecular structure, leaving behind a damaged volume.

Since a large amount of energy is transferred by high LET particles, into a relatively small volume, the multiple collisions or electronic avalanche extends the damaged region, following an exponential law, to about 1000 nm far away from the impinging direction. The resultant size and shape of the altered volume depends on the absorbed ion energy, mass and momentum. This damage is visible under atomic force microscope (e.g. TopoMetrix Explorer, Cf. USA) [21-23]; for practical purposes, the latent damage is chemically etched to form a sufficiently large volume to be visible under light transmission microscope (10x40).

The microscopic process taking place during chemical etching has been described in terms of a dynamic framework governed by capillary condensation [24]; the theory starts from first principles for the description of the microscopic process taking place, and gives physical information on how the inverted cone shaped tracks with curved walls evolve during chemical etching. Deep insight of etched track evolution with complementary information has been reported in literature [25-27]. However, these reports do not contain theoretical framework derived from first principles as developed by Martin et al. [24].

Given the importance for passive track detecting materials and sensitive etching conditions, a set of materials currently employed for photo-neutron field study, are given in Table 1 [28].

**Table 1.** Passive detectors materials, chemical etching conditions, and applications.

| Detecting material | Commecial product | Examples of etching parameters | Aplication (examples) |
|---|---|---|---|
| Polycarbonate (PC) | Lexan | 6N, NaOH 60ºC $t_{etch}$=1 h | Fission fragments |
| | Makrofol | 6N, NaOH 60ºC $t_{etch}$=1 h | Relativistic Lead Ions |
| | Mylar | 6N, NaOH 60ºC $t_{etch}$=1 h | 100 MeV $Si^{8+}$ions |
| Cellulose nitrate (CN) | Daicell | 3-6N,NaOH 60ºC $t_{etch}$=40 m | HEZ |
| | LR-115 | 3-6N,NaOH 60ºC $t_{etch}$=40 m | Interdisciplinary science |
| | CA-80-15 | 3-6N,NaOH 60ºC $t_{etch}$=40 m | Fast neutrons |
| Polyallyl-Diglycol-Carbonate (PADC-NTD) | CR-39™ TASLTRACK-type | 6N, NaOH, 70ºC $t_{etch}$=1-6 h pre-etching 6.25 N KOH, 60% ethyl alcohol at 70ºC 6.25 N KOH $t_{etch}$=12 h | Photo-neutron dosimetry, HEZ, cosmic rays |
| SR-86 Three times more sensitive (in comparision to CR-39™) | (CR-39™ with sulphonate linkages) | 6N, NaOH, 70ºC $t_{etch}$=1-6 h<br>7N, NaOH, 60ºC $t_{etch}$=2-6 h<br>6M, KOH, 70ºC $t_{etch}$=2-6 h | alphas and high energy heavy ions. |
| 0.1% of DOP Dioctylphthalate | Doped CR-39 | 6N, NaOH, 70ºC $t_{etch}$=1-6 h | Space radiation, Proton therapy |

Due to their frequent use in Nuclear Track Methodology (NTM), we report the physical properties of some passive detectors in Table 2 [28].

**Table 2.** Passive detectors employed in NTM.

| SSNTD detectors | Cellulose Nitrate CN | Polycarbonate PC | Polyethylene PET | Columbia Resin CR-39$^{TM}$ |
|---|---|---|---|---|
| Chemical formula | $C_6H_8O_9N_2$ | $C_{16}H_{14}O_3$ | $C_{10}H_8O_4$ | $C_{12}H_{18}O_7$ |
| Density [g cm$^{-3}$] | 1.33 – 1.60 | 1.20 | 1.39 | 1.30 |
| Thickness [μm] | 100-1000 | 75-250 | 100-200 | 500 |
| Uniformity | Acceptable | Good | Good | Good |

**2.1. Radioisotope photon-neutron sources:** The isotopic neutron sources are small, compact, portable and easy to handle. In these sources, a radioisotope is used as projectile source and other material is used as target. The projectiles are α-particles and γ-rays [29].

The $^{252}$Cf is another type of neutron source, where neutron production is due to spontaneous fission [29, 30]. In order to produce neutrons with photons, it is required that the photon energy be at least as large as the neutron binding energy in the nucleus. Target nuclei for radioisotope photo-neutron sources are few since low energy gamma (γ, n) reactions are rare; only two are of interest, i.e. $^{9}$Be(γ, n)$^{8}$B reaction with a threshold energy remarkably low at 1.666 MeV and $^{2}$H(γ, n)$^{1}$H at 2.226 MeV. Table 3 lists most often employed photo-neutron sources, including some physical parameters [31].

**Table 3.** Features of radio-isotopic photo-neutron sources.

| Photo-neutron source | Reaction process | Radioisotope half life $\tau_{1/2}$ | Specific source strength at 1 cm [$10^4$ n/Ci s g ] | Neutron average energy [MeV] |
|---|---|---|---|---|
| $^{88}$Y- Be | $^{9}$Be(γ,n)$^{8}$Be | 105 d | 10 | 0.16 |
| $^{124}$Sb - Be | $^{9}$Be(γ,n)$^{8}$Be | 60.9 d | 20 | 0.024 |
| $^{226}$Ra - Be | $^{9}$Be(γ,n)$^{8}$Be | 1602 a | 3 | 0.50 |
| $^{226}$Ra - $D_2O$ | $^{2}$H(γ,n)$^{1}$H | 1602 a | 1 | 0.12 |

Their importance in research and some specific application is related to their photo-neutron mono-energetic spectrum with well-established (line) energies in opposition to the characteristic broad spectrum of other radioisotope sources (e.g. $^{226}$Ra-Be, $^{241}$Am-Be or $^{252}$Cf). The most often employed radio-isotopic photo-neutron source is the Sb-Be that shows a peak with less that 5.6% energy dispersion [32].

The photo-neutron source strength, $S_v$, can be calculated from the energy distribution of the known photon flux, $\Phi_\gamma(E)$, using the equation 1 [33].

$$S_v = \int_{E_t}^{E_{max}} \Phi_\gamma(E)\, \mu_{\gamma,n}(E)\, dE \qquad (1)$$

Here, $E_{max}$ is the maximum photon energy, $E_t$ is the photo-neutron production threshold and $\mu_{\gamma,n}$ is the ($\gamma$, n) interaction coefficient [34]. The mono-energetic photo-neutron value, $E_n$, is related to the gamma energy, $E_\gamma$, impinging on the target nucleus with atomic mass A, by the following well known equation:

$$E_n = \frac{A-1}{A}\left[E_y + Q - \frac{E_y^2}{1862\,(A-1)}\right] + E_y\left[\frac{2(A-1)(E_y+Q)}{931\,A^3}\right]^{1/2}\cos\theta \qquad (2)$$

Here, Q (MeV) is the neutron separation energy, and θ is the neutron emission angle to the impinging gamma direction. This equation shows some important features: in the centre of mass reference, the photo-neutron has a mono-energetic value meanwhile in the laboratory frame reference, it shows some spreading and depending on the A-value, which may change with angle [34].

Nevertheless, there are other radio-isotopic gamma sources, having target materials always the same, either $^{9}$Be or $^{2}$H. In Table 4, we report a set of them listed in order of increasing average neutron energy [31].

**Table 4.** Mono-energetic photo-neutron sources.

| $E_n$ [keV] | Photo-neutron source | Radioisotope half life $\tau_{1/2}$ | $E_\gamma$ [MeV] | Specific source strength at 1 cm [$10^4$ n/s Ci g] |
|---|---|---|---|---|
| 21 | $^{226}$Ra - Be | 1622 a | 1.69 - 2.42 | 3 |
| 24.8, 377 | $^{124}$Sb - Be | 60 d | 1.69 - 2.09 | 19 |
| 93, 350 | $^{76}$As - Be | 26.1 h | 1.77 – 2.06 | 3* |
| 130 | $^{72}$Ga - $D_2O$ | 14.3 h | 2.51 | 6 |
| 150, 300 | $^{56}$Mg - Be | 2.58 h | 1.77 – 2.88 | 2.9 |
| 184, 484, 750 | $^{72}$Ga - Be | 14.3 h | 1.87 – 2.51 | 5 |
| 197 | $^{228}$Ra - Be | 6.7 a | 2.62 | 9.5 |
| 220 | $^{24}$Na - $D_2O$ | 2.76 a | 2.76 | 13 |
| 220 | $^{56}$Mn -$D_2O$ | 2.58 h | 2.88 | 0.31 |
| 300 | $^{116}$In – Be | 54 m | 2.09 | 0.82 |
| 620 | $^{140}$ La – Be | 40.2 h | 2.51 | 0.3 |
| 830 | $^{24}$Na - Be | 14.9 h | 2.76 | 27 |

* indicates the estimated value

A list of several Q-values [35, 36], and photonuclear cross-section data [37] have been reported. This information gives the possibility to define the passive material response (i.e. etched track histogram) to monoenergetic neutron groups; providing a unique radioisotopic technique for neutron spectrometry study; other option is to use accelerators as monoenergetic neutron source. These are often used for practical applications since they provide photo-neutrons with larger intensity.

In some facilities there are several $^{226}$Ra pellets, as leftover from medical practice, that could be employed as a laboratory source for experimental studies. The $^{226}$Ra needles, applied in the past for cervical cancer treatment, are sealed with a stainless steel cladding. However, if their activities are very high which still makes it suitable, in a properly assembled berylium device, as a low-intensity photo-neutron source. Nowadays, several of them are employed in educational and training laboratories. In Fig. 1, a typical assembly is shown [38].

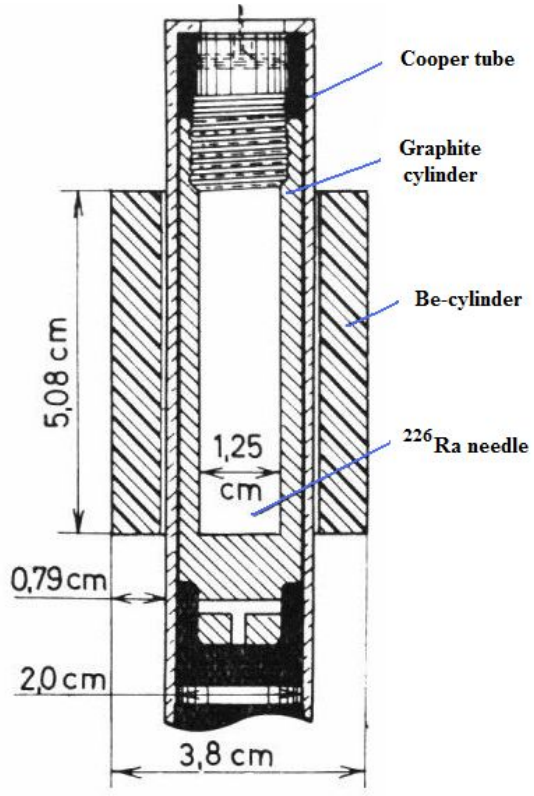


**Fig. 1.** Photo-neutron radium source capsule. The Be-cylinder is containing the $^{226}$Ra needle [38].

Regardless the type of source, it is very important to consider radioprotection aspect when deploying high intensity radiation sources. It is expected also that a proper shielded assembly, for photons and neutrons, is employed for SSNTD exposure [39].

**2.2. Recoils and fragments:** Once the photo-neutrons emission occurs, they are transported to the surrounding space and eventually are absorbed by a given target material or detector. In the case of PADC detectors, neutrons will mainly induce in compounding atoms, proton recoils or reaction fragments depending on the neutron energy. In any case, the energy will be transferred to the target constituents by elastic scattering eventually reaching thermal values due to the hydrogen presence.

During the absorption process, neutrons may also interact with heavier nuclei like the Oxygen and Carbon. Thus, we have to consider the photo-reactions that may also occur, e.g., $^{12}C(\gamma,xn)$, $^{12}C(\gamma,\alpha n)$ or $^{16}O(\gamma,xn)$, especially in the energy window where radiotherapy machines operate (8-25MeV). As a consequence, either the proton, heavier recoils, fragments or reaction products, will leave a latent track in the PADC.

When the neutron source is weak the track density is small. In order to have a higher track density, the detector is covered by a layer of converting material in which specific charged particle reaction conveniently occurs. These materials are selected depending on radiation field under consideration.

One example is the utilization of Boron-10 that finds a large applicability in several interdisciplinary fields [40].

In Fig. 2 are shown the tracks produced by recoiling heavy ions as well as the tracks due to protons.

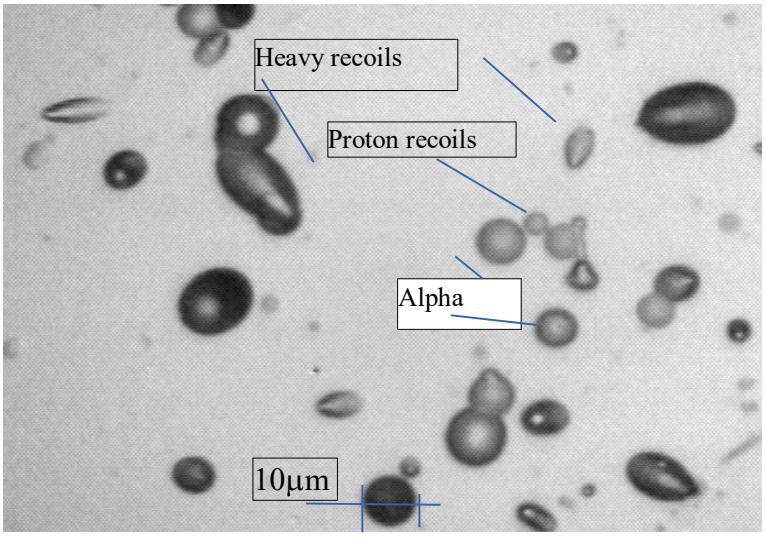


**Fig. 2.** Etched tracks in CR-39 related to recoils and reaction fragments (unpublished).

The other example is related to fast neutrons measurements, $E_n$ > 10-15 MeV; the detector assembly is a sandwiched layer of different detector materials (CR-39$^{TM}$ and Lexan) with converters (aluminium and titanium). Provided with kinetic energy, neutron may induce complex reaction such as: $^{12}C(n, 3\alpha)$. The reaction fragments, e.g. three alpha particles leave a characteristic fingerprint as an etched complex track; these can be properly analysed employing an unfolding technique based on geometrical shape transformation. An example is given in Fig. 3 [41].

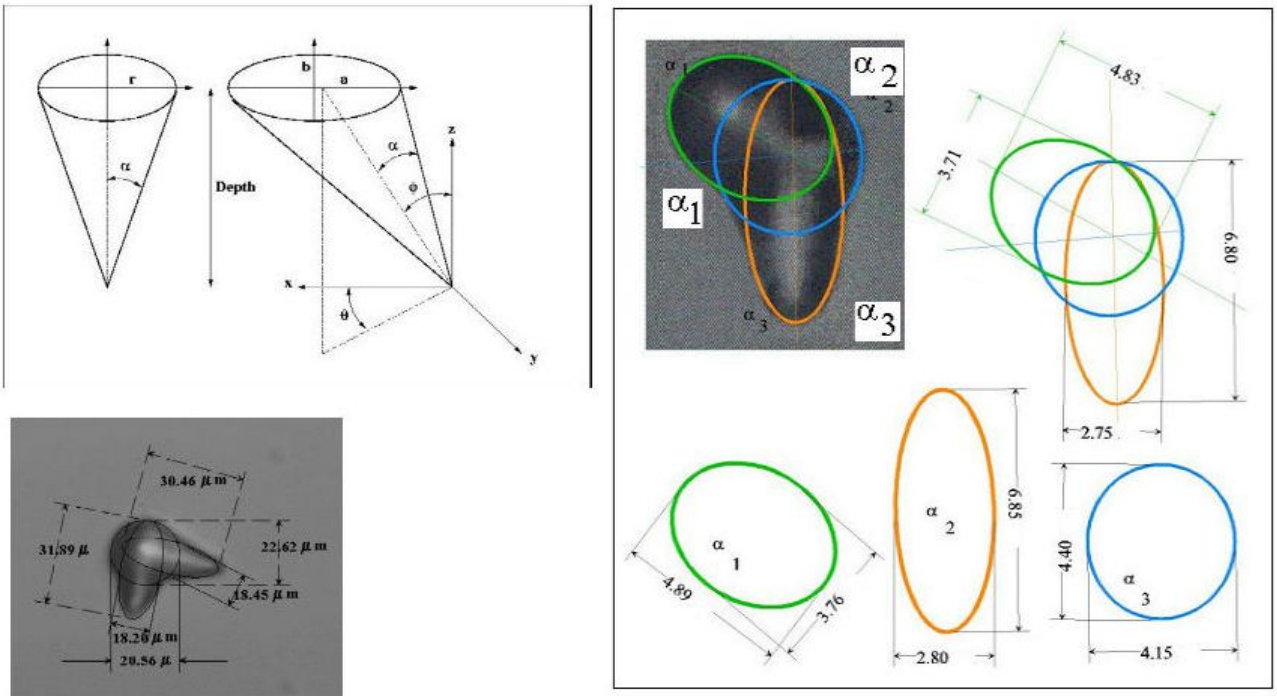


**Fig. 3.** Energetic neutron induced reaction $^{12}C(n,3\alpha)$; etched tracks $\alpha_{1,2,3}$ on CR-39$^{TM}$-TaslTrack-type are identified and the digitized image is unfolded by purpose made algorithm [41].

To visualize the three cone shaped tracks in a 3D frame, simulation programs provide the necessary help to obtain parametrical data; an example is given in Fig. 4.

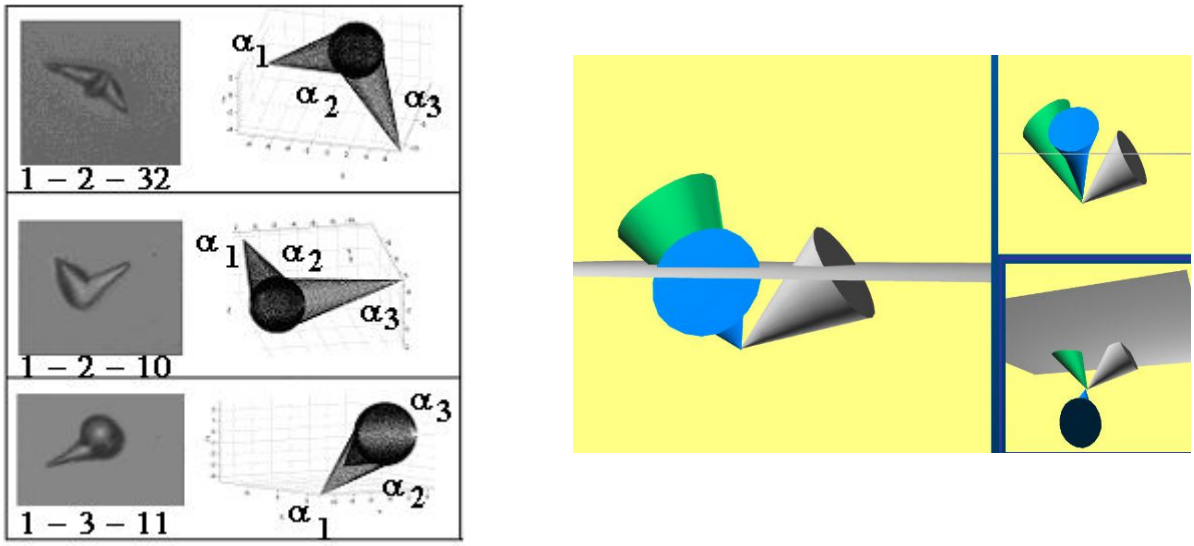


**Fig. 4.** Complex 3-alpha reaction induced by fast neutron visualizaed by etched tracks and its geometrical simulation with SIMPLE 3D sofware [41].

In Fig. 4, the technique is related to fit different ellipses on the track cone surfaces. The circles are then separated to obtain major and minor axes that provide the impinging direction. When these tracks are analysed by programs that simulate their position in a 3D frame, then it is possible to visualize them to determine how they formed during the chemical etching process. The method provides track parameter values for improved data interpretation [41-43].

**2.3. Photo-neutron field detection by CR-39 lined with $^{10}$B converter:** As mentioned above, electron linear accelerators for cancer treatment generate high energy photons that produce photo-neutrons within the $W_{nat}$-target, the Pb and the W in the head, primary, secondary and the multilayer collimators. In order to characterize the photo-neutron spectra and the doses inside the treatment hall, the maze and outside the bunker, experimental procedures using active and passive detectors, and Monte Carlo calculations have been reported [15-19, 35, 36].

In the group of passive materials, several different SSNTDs have been employed. With the use of PADC-NTD, the utility to determine the photo-neutron density at the radiotherapy bunker has been demonstrated. In NTM, the passive detector with the converter is often employed, including cadmium filter in order to determine the ratio between two groups of neutron energy, i.e. thermal and fast. The methodology requires exposing detectors to an expected photo-neutron field at the iso-center, or other sites. Photo-neutrons are indirectly revealed by etched tracks related to proton recoils and alphas from the neutron converter, $^{10}B(n,\alpha)$, or another charged particle reaction. The etching process has the aim to enhance the track, making easier the optical analysis; the etching is already well studied and the chemical conditions were included in Tab 1. The size and shape of the track is distinctive for protons, alphas or ion recoils induced by neutron interactions. In the digital image shown in Fig. 5, the typical tracks related to neutrons can be noticed.

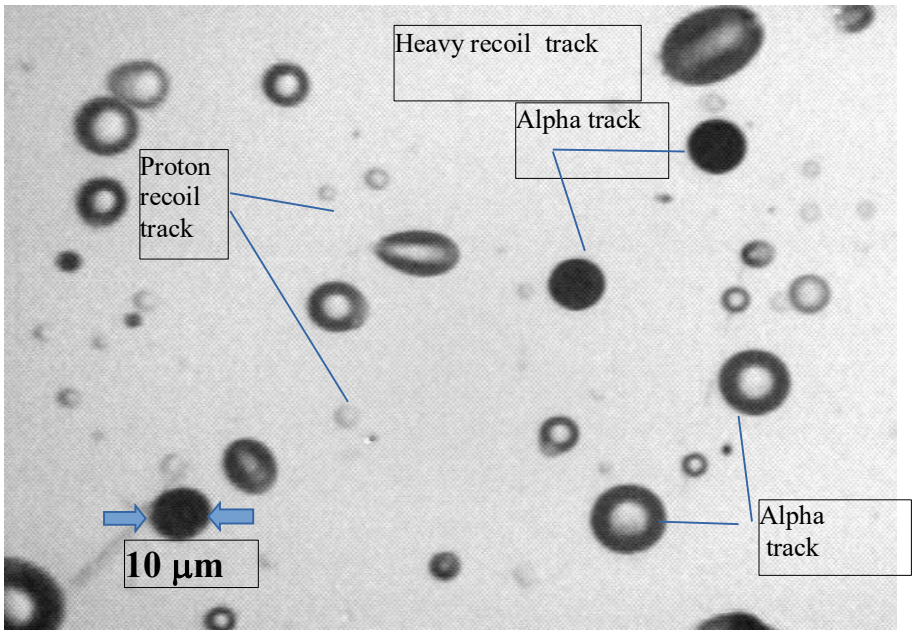


**Fig. 5.** Typical tracks related to $^{252}$Cf fission neutrons recorded in PADC-NTD. These are classified by their diameter and reported in a histogram for further evaluation (unpublished).

Digital images provide track density information. In order to obtain the individual track geometrical parameters and the track density, the digital image must be analyzed. Commercial or homemade systems used for track analysis must provide the following set of track parameters in order to perform intercomparsions [42, 43]:

- *Conversion factors* to determine the real length and the real area of the object
- *Track density*, i.e. the total number of tracks divided by the total scanned area.
- *Track Area:* converted quantity from number of pixels
- *Equivalent diameter*: diameter of a circle having the same area as the corresponding object.
- *Maximum diameter*
- *Perimeter length* or circumference
- *Aspect ratio*: i.e. Eccentricity or Elongation.
- *Shape factor* sometimes called as Roundness
- *Convexity*: real area (pixel by pixel)
- *Orientation*: angle of the major axis of the involving ellipse.
- *Mean Grey level*: derived from the intensity distribution related to software manipulations on the picture such as re-scaling the intensity, contrast increasing, background compensation, among others.

When a track analyser system, automatic or semi-automatic, is used there are several sources of errors [43,44] related to:

1. Optical system. Magnification may be different for type of detectors; these should be using quasi monoenergetic particles and etching them for different times to provide a peaky area distribution.
2. Selection of the light intensity and the condenser system to reduce interference effects. Shape and directional distortion of the tracks is reduced if the optical axis is perpendicularly adjusted.
3. Calibration procedure: to make accurate area or diameter measurements, the horizontal and vertical directions magnifications should be the same to avoid shape distortion.

4. Image processing limitations due to the lack of background compensation and contour enhancement.
5. Segmentation loss due to transformation to binary format. The improperly selected level causes the loss of shallow tracks, truncation or enlargement in the tracks size.
6. Software related to track size and shape selection criteria

One of the commercially available systems for track analysis that has several similar features is the image acqusition device IMAQTM Vision Builder6 made by the National Instruments. The image is collected by a CCD camera and sent to a data acquisition board type IMAQTM PCI/PXITM-1409 (National Instruments). The built in algorithm provides a set of functions, such as the image enhancement, filtration, binary image conversion, pattern recognition, providing frequency histograms for selected track parameters [45].

Analysis of track digital images provides a set of histograms where several groups of tracks can be identified and related to protons and other recoils, or alpha particles. In Fig. 6 are shown the etched track distributions in CR-39 (TaslTrack type) exposed to photo-neutrons.

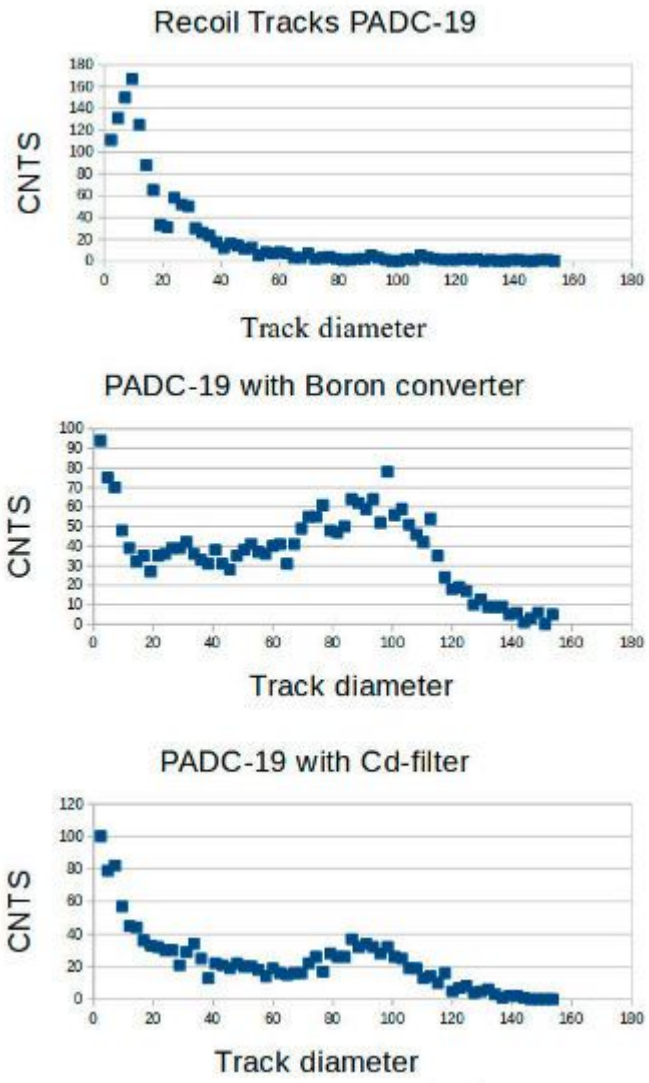


**Fig. 6.** Experimental results on track distribution related to photo-neutrons.

The track distributions are due to protons and alphas. The experiments were carried out at a radiotherapy facility with a Varian Clinac 2300 accelerator (at the GURVE radiotherapy facility,

Caracas, Venezuela) with the aim to determine the photo-neutron intensity and its gradient. In Fig. 6 the obtained track distributions did give out the following information:

- Bare CR-39 detector did show tracks of small area due to recoils (see the Recoil tracks PADC-19, at the top of Fig. 6); these are mainly protons produced by (n, p) scattering due to thermal or fast neutrons. Larger tracks are also noticed and these are interpreted as heavy recoils.
- The next detector, covered with B-converter and Cd-filter, shows a track distribution that has a structure, in fact, lower track area values are due to proton recoils, and the peak is produced by alpha-tracks from the $^{10}B(n,\alpha)$ reaction. The amount of alpha tracks is lesser than the tracks in the detector without Cd-filter. This result, i.e. the presence of an alpha peak due to fast neutrons (we remember that Cd-filter is active in this detector configuration), is justified by the $^{10}B(n,\alpha)$ reaction cross section which is around 3838 b for thermal neutrons but still has high value in the resonance energy region. Therefore, the track distribution (see Fig. 6 bottom histogram, *PADC-19 Cd-filter*) then is related to alpha reaction due to epithermal photo-neutrons. Analyzing further these and similar track distributions related to different detector locations provides data to draw a photo-neutron field map indicating the intensity of thermal and fast neutron region.

The amount of photo-neutrons around Linacs for radiotherapy is relatively small in comparison with the treatment dose, however, its presence delivers an undesirable dose to patient. Due to their radiobiological efficiency and to the neutron interaction with matter features, it has been pointed out as the potential cause of secondary malignancies and cancer recurrence [46-49]. With the aim to estimate the epidemiological risk of treated patients, the photo-neutron level has been measured with PM-355 solid-state nuclear track detectors. In a Varian Clinac 2300 accelerator (at the Oncology Centre in Warsaw), the neutron fluence is $10^6$ n/cm$^2$-Gy. Detectors were calibrated with a bare $^{252}Cf$ neutron source. This procedure provides a proper calibration even when the measured spectra is different from the $^{252}Cf$ [50].

It has been proposed to use a Betatron as a photo-neutron source [51]. A comprehensive study suggesting the use of a Linac as a photo-neutron source has been reported [52]. Other passive detectors, like activation foils, have been used to determine the photo-neutron spectra and the neutron's spatial distribution [53].

## 3. A Resume of Photo-Neutron Converters

Photo-neutrons energy window is inherently characterized by the ($\gamma$, n) reaction mechanisms. At relatively low energy ~30 MeV, the giant dipole resonance (GDR) increases as the photon energy increases, then drops rapidly at larger energies. Due to collective oscillation, the Quasi-Deuteron becomes the dominant process (~150 MeV) [54]. In Fig. 7, the (n, $\gamma$) reaction cross section of deuterium for a wide range of gamma energies is shown. In order to reduce the photon radiation intensity, lead or tungsten is used as a shield in the Linac head as well as other materials whose isotopes have a threshold energy to produce photo-neutrons. In Table 5, the isotopic abundance and the threshold energy of elements in the Linac head is listed [55]. When the bremmstrahlung radiation collides with nuclei photo-nuclear reactions are produced; one of these is the photo-neutron interaction. This is also true when the Linac uses electron beams for therapy, however, the cross section for electro-neutron reactions is approximately 137 times smaller the the cross section for photo-neutron reactions in tungsten [35, 36].

Neutrons leakout from the Linac head reaching the bunker walls and the patient body, also produce some photo-neutron reactions in the patient body. The isotopic abundance and the threshold energy to produce photo-neutrons in main elements in the human body are given in Table 6 [55].

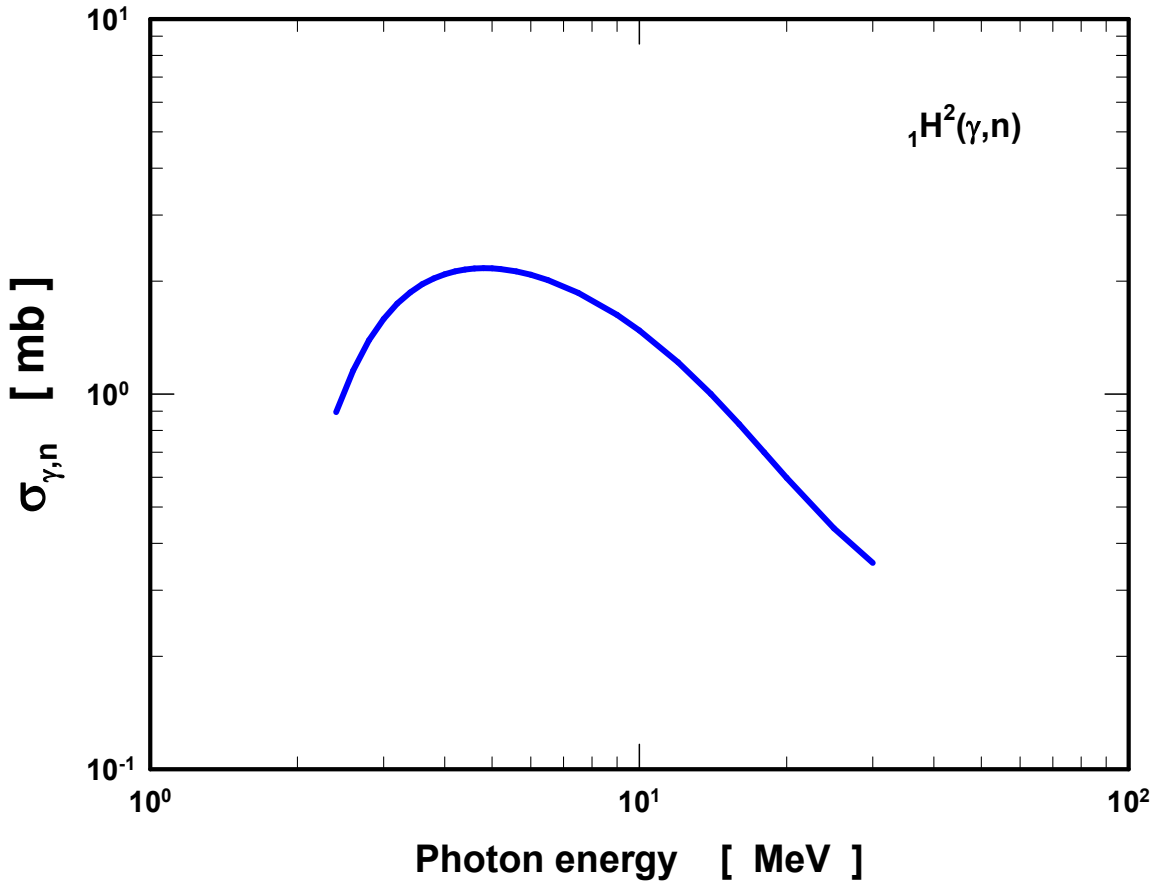


**Fig. 7.** Reaction cross-section σ(γ,n) for hydrogen.

**Table 5.** Isotopic abundance and threshold energy for (γ, n) reactions of elements in Linac head

| Isotope | Abundance [%] | Threshold energy [MeV] |
|---|---|---|
| $^{206}$Pb | 24.1 | 8.09 |
| $^{207}$Pb | 22.1 | 6.74 |
| $^{208}$Pb | 52.4 | 7.37 |
| $^{180}$W | 0.12 | 8.41 |
| $^{182}$W | 26.3 | 8.07 |
| $^{183}$W | 14.28 | 6.19 |
| $^{184}$W | 30.7 | 7.41 |
| $^{186}$W | 28.6 | 7.19 |
| $^{27}$Al | 100 | 13.06 |
| $^{63}$Cu | 69.17 | 10.85 |
| $^{65}$Cu | 30.83 | 9.91 |
| $^{54}$Fe | 5.8 | 13.40 |
| $^{56}$Fe | 91.7 | 11.20 |
| $^{57}$Fe | 2.1 | 7.65 |
| $^{12}$C | 98.89 | 18.72 |
| $^{13}$C | 1.11 | 4.95 |

**Table 6.** Isotopic abundance and threshold energy for (γ, n) reactions of elements in the human body

| Isotope | Abundance [%] | Threshold energy [MeV] |
|---|---|---|
| $^{2}H$ | 0.01 | 2.22 |
| $^{12}C$ | 98.89 | 18.72 |
| $^{13}C$ | 1.11 | 4.95 |
| $^{14}N$ | 99.63 | 10.55 |
| $^{15}N$ | 0.37 | 10.83 |
| $^{16}O$ | 99.76 | 15.66 |
| $^{17}O$ | 0.04 | 4.14 |
| $^{18}O$ | 0.20 | 8.04 |

Primary photo-neutrons are mainly due to evaporation and knock-off reactions. Fig. 8 shows the lethargy spectra of neutrons produced by photons colliding with tungsten [56].

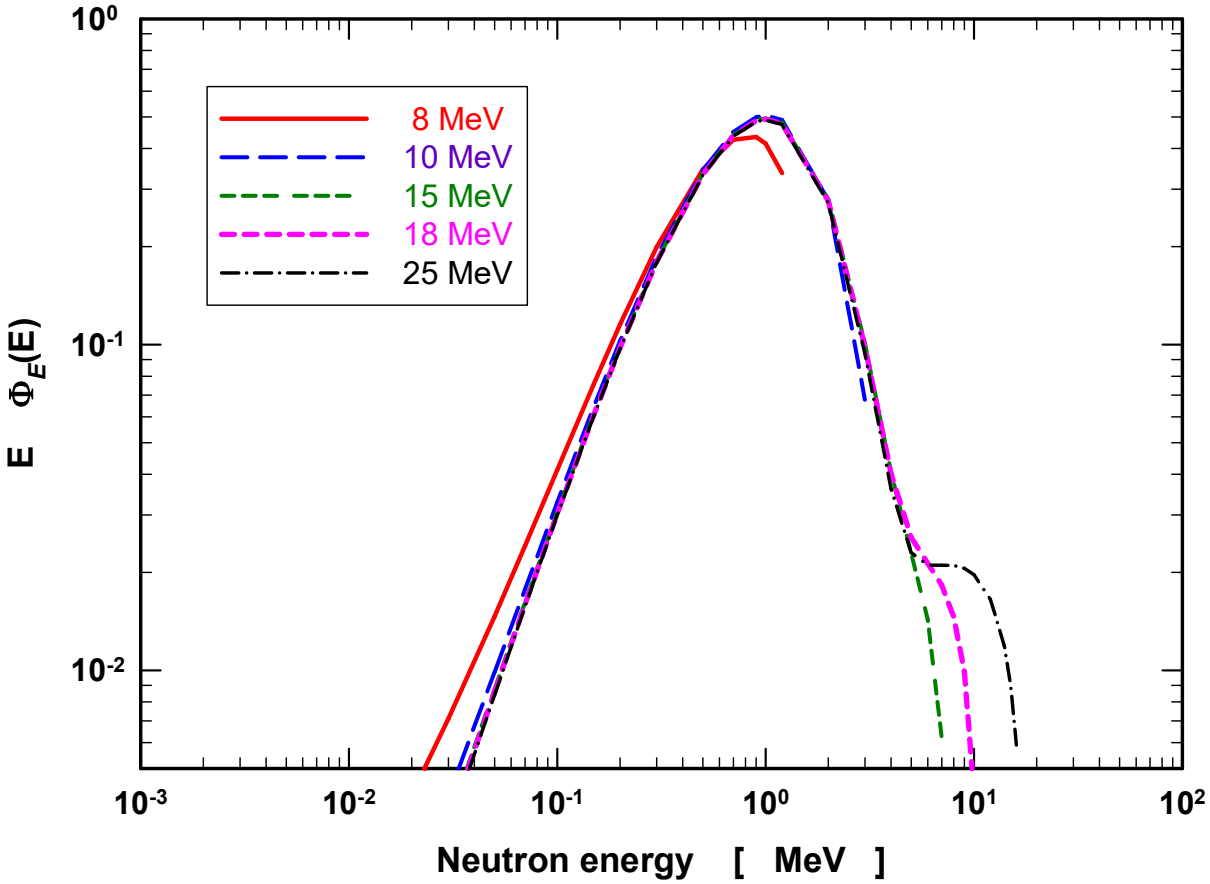


**Fig. 8.** Primary photo-neutron spectra produced in 8-25 MV Linacs.

Through Monte Carlo calculations and experimental methods, the neutron spectra at different locations inside the bunker have been reported [57-61]. In Fig. 9 are shown the photo-neutron spectra at several distances from the isocenter, and at the isocenter plane, as calculated with the MCNP code.

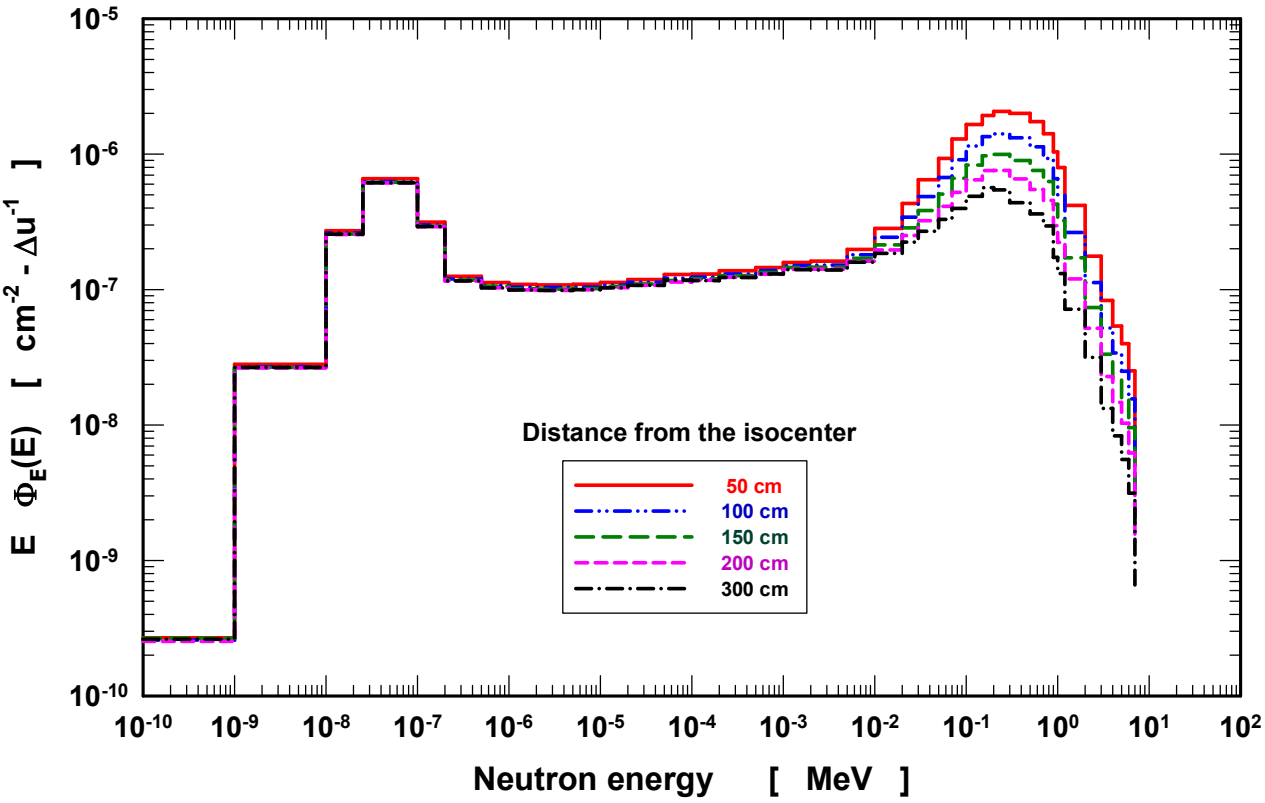


**Fig. 9.** Photo-neutron spectra at diferent distances from the isocenter, produced by a 15 MV Linac.

With the information provided by the neutron spectra, the converter material could be selected looking for materials with high σ(n,x) charged particle. Several materials are employed as photo-neutron converters depending upon the situation, whether the detector is used for dosimetry, spectrometry, or to measure the uranium concentration in tissues [62-67]. In table 7, we report some of them with relevant information.

**Table 7.** Photo-neutron converters reaction and cross-sections (Cd-filter optional).

| Relevant isotope | Reaction | Cross section [b] | Charged particle energy [MeV] | SSNTD CR-39 LR-115, | Reference |
|---|---|---|---|---|---|
| $^{3}$He<br>H (n,p) scattering | $^{3}$He (n,p) $^{3}$H | 5333 | 0.573 (p); 0.191 ($^{3}$H) | beam geometry, area and accident dosimetry. | Palfalvi and Bhagwat et al. [62] |
| $^{6}$Li | $^{6}$Li (n,α) $^{3}$H | 940 | 2.727 ($^{3}$H); 2.050 (α) | glass dosemeter containing lithium | Savvidis et al. [63] |
| $^{10}$B | $^{10}$B (n,α) $^{6}$Li | 3838 | 1.470 (α); 0.80 ($^{7}$Li) | Area monitoring. $^{10}$B implanted in silicon+CR-39<br>Glass metal Fe(75%)$B_{nat}$(25%) | Izerrouken et al. [64]<br>Alvarado et al. [65] |
| ($Li_2B_4O_7$) | $^{10}$B (n,α) $^{6}$Li<br>$^{6}$Li (n,α) $^{3}$H | 3838 | 1.470 (α); 0.80 ($^{7}$Li) | Glass converter neutron field monitor | El-Sersy et al. [66] |
| $^{235}$U | $^{235}$U (n,fis) | 600 | ~200 MeV fis$^{-1}$ | Human tissue | Hassen et al. [67] |

In Table 7, the (n, p) reaction on He-target is not employed as converter for SSNTD, however, it could be an interesting experiment to employ it for simultaneous detector response to different particles mass, i.e. protons and tritons. The most often employed converter is by far the Boron, either employed in elemental form or chemical compound, sometimes having enrichement close to 100%. An application worth to mention, is the employment of glass metal (Fe75% B25%) [68] converter in which alpha particles and the lithium ions produce highly ionized molecules in the immediate vicinity of the reaction; NTM open the way to study neutron damage or dislocation of atoms and quality control by autoradiography of Boron distribution. Though almost all the nuclear reactions producing charged particles in principle could be emloyed as neutron converters, only selected isotopes are employed depending on specific application. We already mentioned the most recurrent application, nevertheless, the others have been sucessfully employed. One of the complex detector converter assemblies employed in high energy neutron field are reported in Figs.10 (a) [68] and 10 (b) [69].

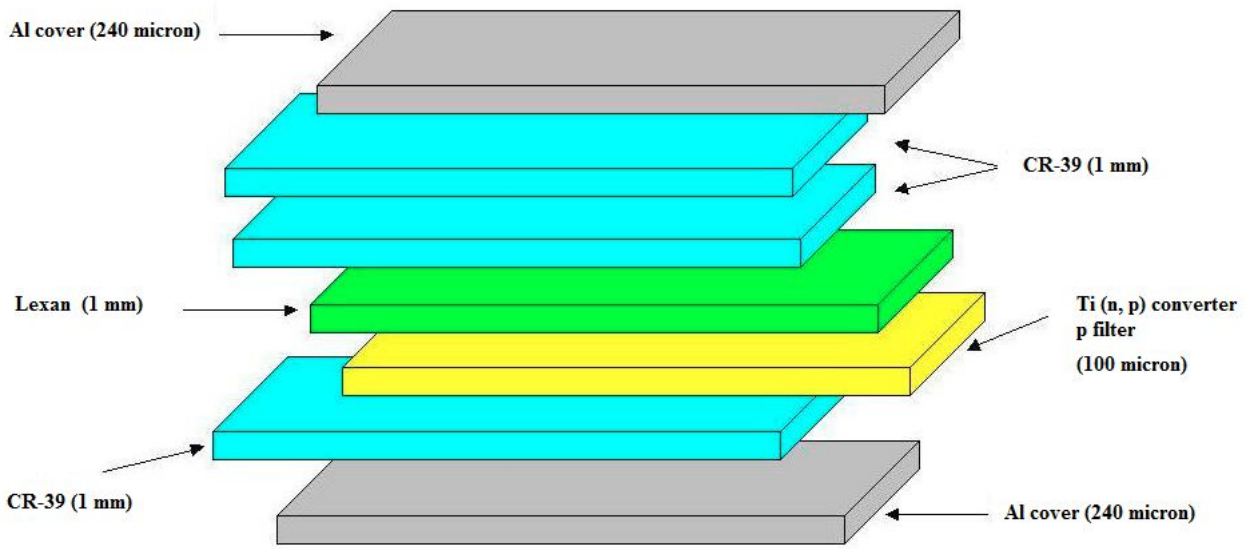


**Fig. 10 (a).** Track detectors and converters assembly for energetic neutron and proton responses.

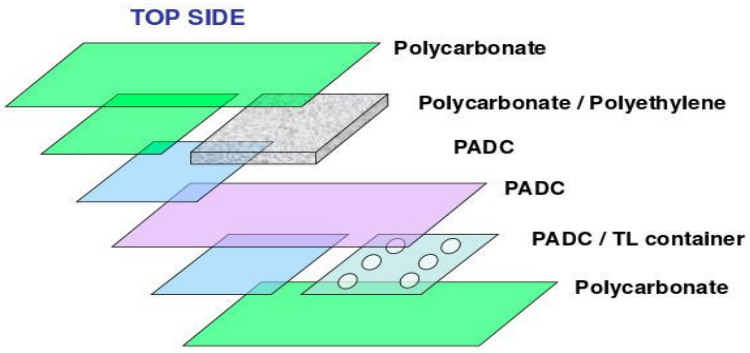


**Fig. 10 (b).** Track detectors assembly for mixed radiation field.

**3.1. Determination of photo-neutron fluence rate:** A large set of results are today available on the neutron response function of SSNTD materials. In this case the most important factor setting any experimental value is to establish the chemical condition for latent track visualization. The second point is the converter material, either the detector itself as often reported, or combined with charged particle reaction having a relatively high reaction cross section. The calibration methodology often

relies on isotopic neutron source such as the mentioned $^{252}Cf$ with a well-known fission neutron spectrum that follows the Watt function, or Ra-Be with a broad energy spectrum.
It is expected that the calibration curve be a straight line once the detector system efficiency is known. In case of Linac induced photo-neutron sources, the neutron spectrum is often below 0.51 MeV and tracks are related to elastically scatted protons due to CR-39$^{TM}$ hydrogen rich compound. For the fast component of the neutron spectrum, El-Sersy et al. [66] obtained an efficiency value of $\varepsilon = 3.1 \times 10^{-5}$ tracks/neutron, probably employing cadmium filter as a cut-off for thermal neutrons. The etched track density must be a linear function of the neutron flux $\rho$ (tracks cm$^{-2}$) even if converter reaction is included. In this case, the detector efficiency $\varepsilon$ will depend on the reacting isotope concentration of, e.g., Boron-10. As mentioned above, some contribution also comes from (n, p) and (n, $\alpha$) reactions within PADC constituents, i.e. C, N, and O. Nevertheless, in the value of the calibration factor this interfering term is taken into account by the removed layer. Depending on the etching condition, as expected, different values are obtained, e.g. the calibration factor is $\varepsilon = 6.2 \times 10^{-5}$ track/neutron for CR-39 etched by 6N NaOH at 70ºC. Then the photo-neutron fluences are affected by the applied NTM for track density conversion to fluence. Kumar et al. [70] after several measurements with etching conditions of 7N NaOH at 60ºC, report $\varepsilon = 1.2 \times 10^{-3}$ track/neutron. Matiullah et al. [71] concluded that for calibration of CR-39$^{TM}$ detectors for dosimetry, the calibration source must have a similar shape to the spectrum to be measured since a dependence on the neutron energy exists. For CR-39$^{TM}$ calibration, 4 isotopic neutron sources are recommended: bare $^{252}Cf$, $D_2O$ moderated $^{252}Cf$, $^{241}$Am-Be, and $^{241}$Am-B; the track efficiencies are $5.28 \times 10^{-4}$, $1.35 \times 10^{-4}$, $8.92 \times 10^{-4}$ and $6.66 \times 10^{-4}$ track/neutron, respectively, for chemical etching [72].

**3.2. PADC calibration methodology:** To visualize latent track, a chamical etching is required. The process is based on the bulk etching velocity $V_B$ being lower that that corresponding to the damaged volume, i.e. track-etch velocity, $V_T$. Their ratio indicated by $V = V_T / V_B$ is a variable parameter depending on the chemical composition, etching conditions and LET of energetic particles [73], other than manufacturing or curing cycle and dopant. Most laboratories either for calibration or measurements rely only on keeping constant the etching parameters and then measure directly the removed thickness, $\Delta h$. However, it has been pointed out that this approach may lead to large uncertainties [74]. Therefore, a new method was suggested for $\Delta h$-value measurement based on etched track diameter exposing passive detectros to collimated monocromatic alpha source. The calibration methodology consists in obtaining etched track histograms employing an advanced image analyzer; from that precise values $\Delta h$, V and LET with their errors could be deduced. In this case, a set of ion beams were available at the HIMAC accelerator of National Institute of Radiological Sciences (NIRS, Chiba, Japan) and PADC detectors. The expression reported by the mentioned authors is:

$$V_T = 1.0189 - 1.0185 e^{-d/11.17}$$

where d is the track diametrer in μm. The most important outcome is that it provides the value of removed layer thickness also if track becomes over etched. The bulk velocity experimental value is $V_B = 1.34 \pm 0.03$ μm h$^{-1}$ and $V_T = 6.87$ μm h$^{-1}$ at the Bragg peak for 6N NaOH at 70ºC. For a higher NaOH concentration, $V_B$ and $V_T$ values for CR-39 $^{TM}$ detector using 6.25 N NaOH at 70$^0$C are 1.62 μm/h and 5.24 μm/h, respectively.

**3.3. Photoneutron dose assessment:** NTM with passive system is one of the techniques selected to establish dose equivalence of a fast neutron field without knowledge of the neutron energy spectrum. Therefore, it provides information also on neutron induced radiation risk level due to the photo-neutrons. The poly-allyl diglycol carbonate (PADC) neutron dosimeter provides doses up to 250 mSv (Health and Safety Executive, HSE), in the neutron energy range (144 keV to 15 MeV) for controlling the radiation in work places. This passive neutron dosimeter offers a relatively simple method since neutrons interact mostly by inelastic scattering, elastic scattering and absorption, leaving latent track NTD. For convenience, PADC type CR-39$^{TM}$ ½ cm thick are used to determine neutron dose around the experimental facility due to their sensitivity to charged particles that induce

localized damage forming latent track. It is expected that these are produced by charged particles due to (n,p) and (n,α) reactions. After the chemical etching, tracks were counted and track geometry was determined employing MORFOL analysis program [75]. The amount of tracks per unit surface (tracks/$cm^2$) was converted to a neutron dose (10.2 ± 0.7 track $cm^{-2}$-$mSv^{-1}$ or specific calibration of 1.2 tracks/mSv), from which neutron dose and its anisotropy was obtained.

## 4. Historical Aspects and Linac Future

In 1939, a reaction mechanism was suggested for photo-neutron production [76]. Later on in 1953, the mechanism was experimentally confirmed using photographic plate technique to obtain the cross section as function of the impinging photon energy [77]. The photoneutron cross sections of some elements were reported [78, 79] during the following decades and photo-fission captured the general interest for heavy elements mainly $^{238}U$ and $^{232}Th$ from 5 to 8 MeV. An interesting review on Linac for medical treatment is published by Thwaites et al. [80]. The authors review the early history and development of linear accelerators for patient treaments. After the first medical treatment was carried out at the Hammersmith Hospital in London back in 1953, as new technologies emerged they were introduced for improved devices and with time Linacs entered the medical radiation therapy and diagnostic field.

Cancer treatment is carried out with ionizing radiation alone, or combined with surgery and/or systemic therapy including chemical, immunological and genetic therapy. Radiation is applied as systemic radiotherapy as teletherapy or brachytherapy. In teletherapy, a radiation beam is addressed to the patient aiming at killing cancer cells without affecting the normal tissues around the tumor. Thus, the classical radiation therapy, CRT, was improved to 3D-CRT, evolving to Intensity-Modulated Radiation Therapy, IMRT. Changes included the multi-leaf collimator system, MLC, and advanced optimization algorithms [81].

Despite the fact that there are several options for cancer treatment, radiotherapy with Linacs is the technique most commonly used, either with electron or photon beams [82]. A lower skin dose, a higher depth dose, a reduced scattered dose to healthy tissues outside the tissue-target volume, and less rounded isodose curves, are some of the advantages provided by the use of high-energy x-rays instead of low energy photons produced in a Linac [83]. However, the use of high-energy photons becomes a radiation protection issue. Besides the therapeutic beam, Linacs produce neutrons that induce reactions in materials inside the bunker, such as activation [84] and prompt γ-ray reactions. Neutrons deliver an undesirable dose to the patient; this dose can cause secondary cancers. Working above 8 MV, Linacs produce neutrons regardless of the fact that they operate with electrons or x-rays. In case of electrons, neutrons are produced via virtual photon reactions (e, e'n), while x-rays generate neutrons in (γ, n) nuclear reactions. Cross section for photo-neutron production is larger than for electro-neutron production, therefore studies have been focused on photo-neutrons [85-88].

The neutrons emitted by photo-nuclear process have two peaks, one around 1 MeV, produced by the evaporation of the excited nucleus, the other at higher energy due to a so called direct reaction mechanism. In spite of knowing the photo-neutron production with mean energy of a few MeV, it has been not considered as a risk to the patient during treatment, however, neutrons are considered during the bunker design in order to reduce the dose to general public and radiation workers. However, it has been reported by Martin et al. [89] that the children should not be treated by Linac operating above 10 MV. However, cancer patients globally that undergo radiation therapy is increasing in number and that will stimulate the accelerator market. As significant technological advancements are in sight, specialists already forecaste that by next year (2016), the business will try to reach the staggering amount of $3.7 billion. Even if Siemens recently announced to abandon the Linac production, other companies such as Varian Medical System (US), Swedish company

Elekta AB, Accuray (US), IBA Group of Belgium, Eckert & Ziegler BEBIG, iCAD, Inc., GE Healthcare, Covidien and other more will have the opportunity to have a larger share [90].
Linacs for therapy have been evolved along the time, initially the treatment area was square or rectangular where together with the tumor the sensible tissue and organs around the malignancy received the dose. A breaktrough was the use of the multileaf collimator (MLC) that is a set of tungsten leaves that allow sharpening of conformal or intensity-modulated fields in Intensity Modulated Radiation Therapy. The MLC leaves have complex designs for the leaf ends and the leaf edges. During treatment, the MLC leaves can move during beam delivery in step-and-shoot and dynamic treatments, thus the treatment beam adopts the tumor area reducing the dose to organs and tissues. The drawback of MLC is that a larger amount of photo-neutrons are produced. A new technology is the tomotherapy with 6 MV linacs, where apparently there are no photo-neutrons and very precise doses are delivered, however, it is necessary to carry out more research with these new Linacs.

## 5. LINAC Sources and SSNTDs

Photo-neutrons are mainly produced in the high-Z materials on the Linac head such as the target, the flattening filter, the jaws, the MLC, and the head shielding; also, they are produced in the patient body and materials in the treatment hall whose cross sections show the Giant Dipole Resonance (GDR) [55]**.** Fig.11 shows the microscopic cross sections of some isotopes for GDR in the range above 8 MeV.

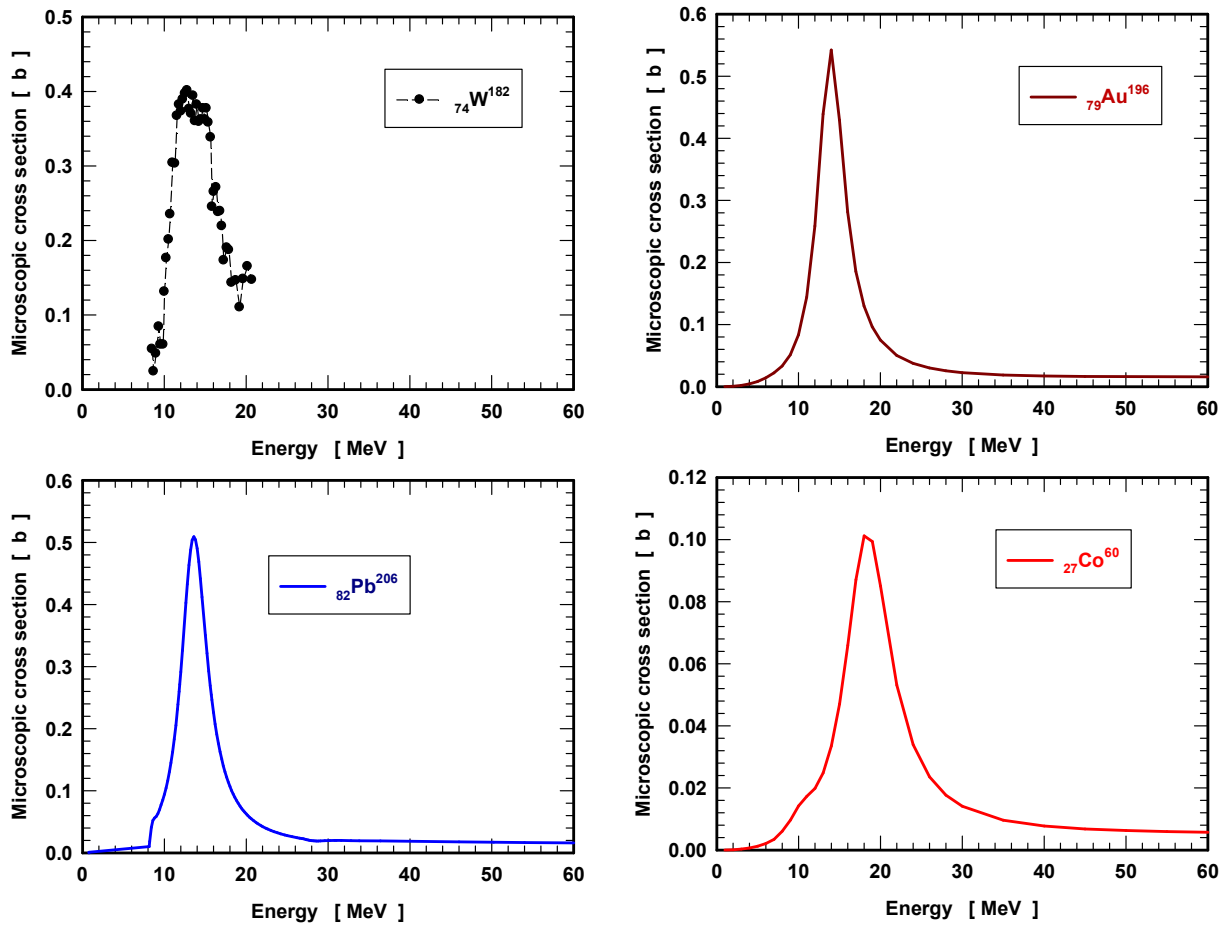


**Fig. 11.** Microscopic cross sections with the GDR.

In high-intensity, mixed and pulsed neutron fields the use of spectrometers or area monitors with passive detector have several advantages over active systems. Several works have been carried out

with the aim to characterize the photo-neutron spectra around LINACs for radiotherapy. Inside the treatment hall, the radiation field is intense, mixed and pulsed, therefore, the use of instruments based on active detectors is not reliable. To overcome this drawback, passive neutron detectors have been used. Thus, in order to measure the neutron fluence rate, the neutron spectrum and the doses, foil activation detectors, pairs of thermoluminescent dosimeters, bubble detectors and track detectors have been used.

Around Linacs, it is advisable to measure the neutron spectra, however, the use of a neutron spectrometer with a passive detector takes long time. In order to overcome this drawback, a method named planetary method has been developed that requires a single shoot from the Linac. For this two conditions need to be reviewed: the neutron field symmetry and the cross-taking among the spheres [57]. Another option is to use a passive neutron area monitor to measure the ambient dose equivalent. The response of a neutron area monitor made of polyethylene with a CR39 and with $^{10}B$ foil as converter has been estimated with Monte Carlo methods [91].

The use of spectrometers, neutron area monitors, or neutron dosimeters around Linacs for radiotherapy is a forced condition due the radiation field features in the treatment hall. When TLDs are used as neutron detectors, the photon field is considered by using pairs, with TLDs sensitive to photons and neutrons, and TLDs sensitive to neutrons. Activation detectors, like Au or Dy [92, 93], and the SSNTDs are not affected by the presence of photons. Once the foil is activated the induced activity must be measured on-site, on the other hand, the SSNTDs can be analyzed later on under the controlled laboratory conditions, and the only feature that must be considered is the effect of the Rn in the environment. This drawback can be overcome by protecting the SSNTD since its irradiation until its analysis and using detectors to measure the background. However, it should not be an issue since measurements take place only for time intervals of minutes.

**5.1. Neutron surveillance at Linac facilities with PADC:** Nevertheless the SSNTD is a mature technology but several areas need improvement, for example, to obtain the neutron spectrum instead of total neutron fluence or a dose value based on a single calibration factor. Other areas that require more research is the use of new algorithms, or techniques based upon artificial intelligence for image analysis, to evaluate the response when converters and filters are included. New dosimeter could be developed employing the already well developed NTM to measure the additional dose received by patient under treatment. That, in some cases, requires several dozens of treatment and the passive system could be employed to determine the neutron component dose for two groups of photo-neutron field (thermal and fast). For this purpose, sandwich detectors similar to that given in figure 10 (b) could be employed wih the modification that Boron-10 converter and Cd-filter is to be introduced. This new dosimeter could be developed since the neutron spectrum is quite well established, as well as the detector response to photo-neutrons either by experimental or simulation studies.

For illustration, we give in Fig. 12 a possible sandwiched dosimeter suggesting a modified scheme of one given in figure 10 (b). This system could well be applied also for ambient neutron dose or as neutron surveillance passive PADC-system inside the halls of Linac driven radiotherapy facilities.

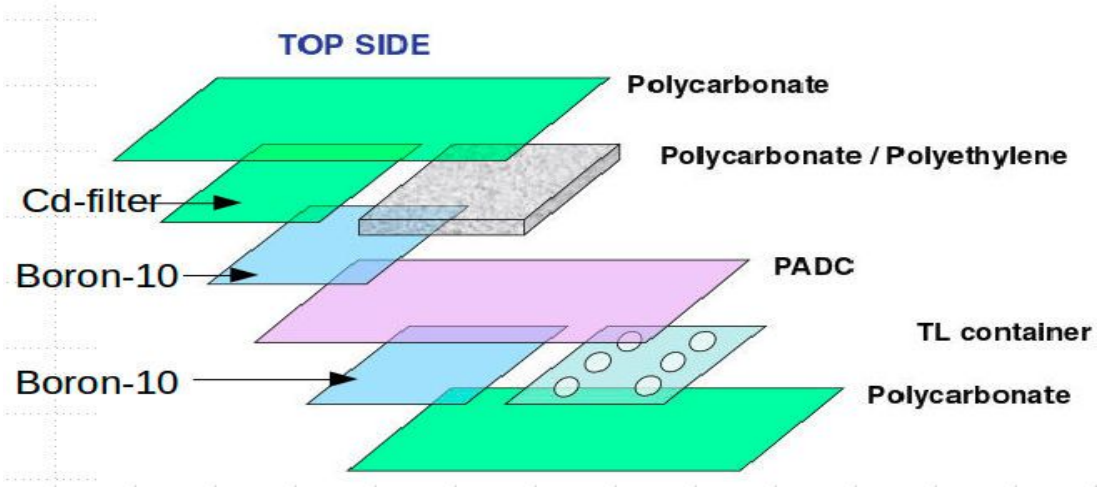


**Fig. 12.** Photo-neutrons dosimeter employing PADC, sandwiched with Boron and Cd, as an improvement on Szabo´s scheme of Fig. 10 (b).

**5.2. Neutron dose at particle accelerator workplaces:** Neutron dosimetry based on PADC copes with the requirement to measure doses from neutrons to the whole body and to the skin in terms of the radiation quantities Hp(10) and Hp(0.07). Technical specification copes with dose values in the range 0.2-200 mSv. Exposure interval is 1-3 months depending on the workplace. Detector responds to an energy region that stands in the range of thermal, epithermal and fast neutrons, i.e. 144 keV – 15 MeV. The neutron lower energy is related to the threshold required to produce a latent track; above 144 keV upwards are detected by direct collisions with nuclei in the dosimeter/holder assembly, whilst the detection of thermal neutrons utilizes capture interactions with nitrogen nuclei in the nylon holder. Hence, the detector is able to detect neutrons over a very wide energy range; the neutron dosimetry service is approved by the Service of Public Health England under Regulation 35 of the Ionising Radiations Regulations 1999.

The neutron dosimeter is subject to measurement uncertainties that have to follow European Commission report Radiation Protection 160 related to Technical Recommendations for Monitoring Individuals Occupationally Exposed to External Radiation. Detector performance tests are typically 10% (well below the recommended values). One of the main advantages is that the passive etched detector can be stored for several years and it can be analyzed again over the time without loosing information of dose values since its fading is negligible due to ambient heat or humidity.

Other published work assessed the quality of PADC for personnel dosimetry of both photo-neutrons and neutrons produced by Thermo Electron (USA), Track Analysis System Limited (UK), Chiyoda Technol Corporation (Japan) and Intercast SRL (Italy) [94].

Tests were made exposing the dosimeters to a personal dose equivalent of 3 mSv in the field of a $^{241}$Am-Be source to provide assessment of the variation of neutron sensitivity and background signal. We report results that show the variability; we have to state that the digitized image analyzers may alter track size reading and may introduce large errors. In this case, probably the TASL-Image track analysis system was set neglecting superposed tracks or too small sizes; that could justify data dispersion given in Table 8 [94]. Therefore, it is a good practice to participate often in intercomparison exercises (refer to section 2.3).

**Table 8.** Data comparison on SSNTD dosimeter quality by manufacturer.

| PADC manufacturer | Sensitivity $cm^{-2}$ $mSv^{-1}$ | Average Tr $cm^{-2}$ | Bkgd tracks $cm^{-2}$ | Dose mSv |
|---|---|---|---|---|
| TE | 460+/-47 | 1379+/-13 | 29=/-17 | 0.16 |
| Tech-1 | 256+/-27 | 767+/- 12 | 117+/- 61 | 0.97 |
| Tech-2 | 316+/-32 | 930+/-7 | 10+/-7 | 0.10 |
| TaslTrack | 226+/-24 | 678+/-11 | 19+/-19 | 0.35 |
| Intercast | 733+/-74 | 2159+/-14 | 66+/-21 | 0.12 |

**5.3. Measurement of the beam exit of In-hospital Neutron Irradiator:** Accelerator based treatment of glioblastoma tumours cope with the requirements of high dose rates to the brain targeted region with epithermal neutrons of ~ $10^{13}$ n $cm^{-2}$ [95]. Neutron therapy application such as Boron neutron capture therapy (BNCT) requires higher flux and conveniently low power reactors are employed; thermal neutron flux at selected beam tube exit may produce ~$1x10^{9}n/cm^{2}s$. Available reactor therapy doses are thermal neutrons of ~$10^{-11}$ cGy/(thermal fluence) and epithermal neutrons flux at a properly designed tube ~$5x10^{8}n/cm^{2}s$ with a dose rate of fast neutrons of $2x10^{-12}$ cGy/(epithermal fluence) [96].

**5.4. Passive detector method for secondary neutron field measurement:** Dedicated Linac for medical treatment, other than the primary radiation, produce photo-neutrons far-out-of-field region. Measurements of the secondary neutron average field and its contribution to the absorbed dose has been studied by different authors [89, 97], which did show the overall effect to the patient during treatments; the lowest is for ions delivered by scanning, the highest is related to IMRT collimators and the middle is the passive modulation. Linear accelerators have been compared on available technical data by Howell et al. [98], to assess photo-neutron production. The driving motivation was the concern that the secondary neutron field varies depending on photon beam energy, materials and technical design.

The technical data of Linac often are not disclosed by the manufacturer of the accelerator objecting that it is not policy of the company to release specific information. This is quite an obstacle when data on target design and material is a compulsory input for simulation. Consequently most of the studies related to modelling multileaf collimators, photo-neutron spectra or total neutron fluence to estimate ambient dose equivalent and neutron source strength produce results having large uncertainties. However, direct measurement employing either active or passive metodology provides sufficient insight for proper data from which important concluisons can be drawn. An alternative hybrid approach [99] was proposed to overcome these and other technical difficulties for neutron absorbed dose estimation (which is based on Monte Carlo and exact methods).

The main result is that the non-elastic reactions account for a probability weight of 72.54% and its fraction in the total absorbed dose has a range between 91% (breast) and 98% (lung). Measurements with NTM offer the possibility to determine the gradient of the fast neutrons around a radiotherapy hall. The following alpha track histogram is an illustration of the capability of the passive method with converter and cadmium filter. From the sequence of track histogram (Fig.13), the gradient of the neutron field can be observed as the position is changing. The top histogram shows a zone where photo-neutrons have an intermediate component between thermal and fast neutrons; the second and the bottom are related to a neutron field dominated by thermal and fast components, respectively. Histograms are obtained substracting the proton and heavier components and considering the cadmium filter so that the fast component and the thermal one are conveniently separated. This technique is important in the case of neutron field characterization around the fusion plasmas [100].

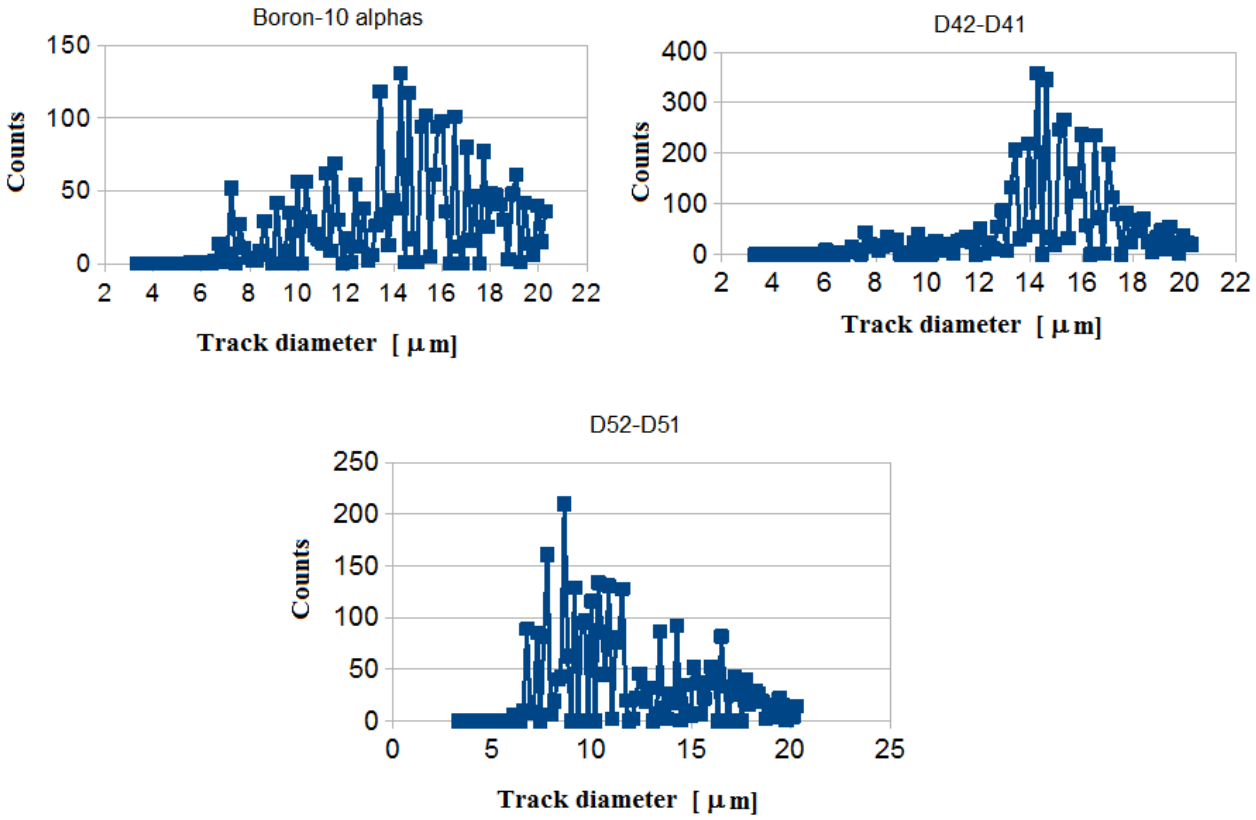


**Fig. 13.** Passive detector histogram (identified by letter and number) showing secondary neutron field measurements for three different locations in a radiotherapy hall.

## 6. Computer Simulation

The design of a neutron detector is often made using Monte Carlo methods. There are some Monte Carlo codes that are available like: Geant4, Fluka, MCNP, Morse, SRIM, etc. The Monte Carlo method (MCM) is based on two theorems: the law of large numbers and the central limit theorem [101]. Instead of solving the radiation transport equation, the MCM emulates the radiation transport in matter. The use of Monte Carlo requires designing a model as close as possible to the real situation. In the model, the radiation transport is simulated requiring a good set of validated cross sections and a good random number generator. The response of neutron spectrometers with passive and active neutron detectors have been calculated with different Monte Carlo codes [102-107].

The MCNP4C code has the extended capability for solving neutron, gamma, and electron problems [108], and SRIM is a well-known Monte Carlo code used for ion transport calculations [109]. Both codes have been used to estimate the efficiency of CR-39$^{TM}$ with polyethylene and aluminium covers. A FORTRAN program, named FTRAC, was developed to determine the specifications of recoil protons using the kinematics of interactions and the PTRAC card produces an input for SRIM code where the proton transport through the radiator is simulated obtaining the tracks registered in the CR-39$^{TM}$ detector. The polyethylene was used as radiator, and the aluminium was used as degrader [110].

Fast neutrons produce intrinsic tracks in detector as a result of elastic scattering reaction of neutron with the SSNTD constituents, especially hydrogen nuclei. In order to increase the detector efficiency, a thin polyethylene plate is used as a recoil proton source. The technique of energy-selective fast-neutron detection is based on the track density measurement in CR-39$^{TM}$ detectors

placed in contact with a variable thickness of degrader. Materials like lead, aluminium or gold are less likely to have (n, ion) reactions followed by a polyethylene radiator. In order to produce a track in the CR-39$^{TM}$ detector, the recoil protons from the polyethylene radiator must have enough energy to pass the degrader and fall within a definite energy window [111-113]. The advantage of measuring the neutron spectrum is that any dosimetric quantity can be estimated. However, the measurements take long time being inconvenient for some radiotherapy facilities with Linacs. An option is to use PADC foils with a polyethylene and PVC radiator to measure the Hp(10) [114]. Other option is to use a passive neutron area monitor to measure the ambient dose equivalent [115]. Using the MCNPX code [116], the response function of a neutron area monitor with CR-39 was calculated. The CR-39 was sited at the centre of a 20.25 cm x 20.22 cm height polyethylene moderator. In the model, the polyethylene terephthalate support, the CR-39$^{TM}$ and the $^{10}$B (100%) were included. The response, in terms of (n, $\alpha$) reactions in $^{10}$B, was estimated for 47 mono-energetic neutrons from $10^{-10}$ to 20 MeV [91].

## 7. SSNTDs in Fusion Studies

A convenient tool in deuterium plasma diagnostic is NTM by SSNTDs for Plasma-Focus, Tokamak, and laser-plasma-experiments among others, because of its insensitivity to electromagnetic noise and cope with ability to distinguish the types and energies of individual high LET charged particles [5]. Passive detectors are therefore a direct indicator of reaction products, especially neutrons, and provide an alternative diagnostic techniques for fusion machines. CR39$^{TM}$, PM355, LR-115 have been tested to provide rate values of nuclear reactions occurring in plasma, the location of fusion-reaction sources, parameters on thermal data and accelerating mechanisms in fusion processes, angular anisotropy of fusion-reaction product streams, etc. It has been shown that these devices could cope, without loss of information, with fluence-values well above of $1.3\times10^{11}$ neutron/shot to provide imaging of fusion protons.

Seguin et al. [100] employed 50μm thick Kapton window to record fusion reaction products such as 2.45 MeV neutrons and 3.03 MeV protons. The window foil has such a thickness that it is almost transparent to these particles, but shields at the same time the SSNTD from the plasma of 1.01 MeV tritium and the 0.82 MeV $^{3}$He nuclei. For the sake of illustration some of the related etched tracks are given in Fig. 14.

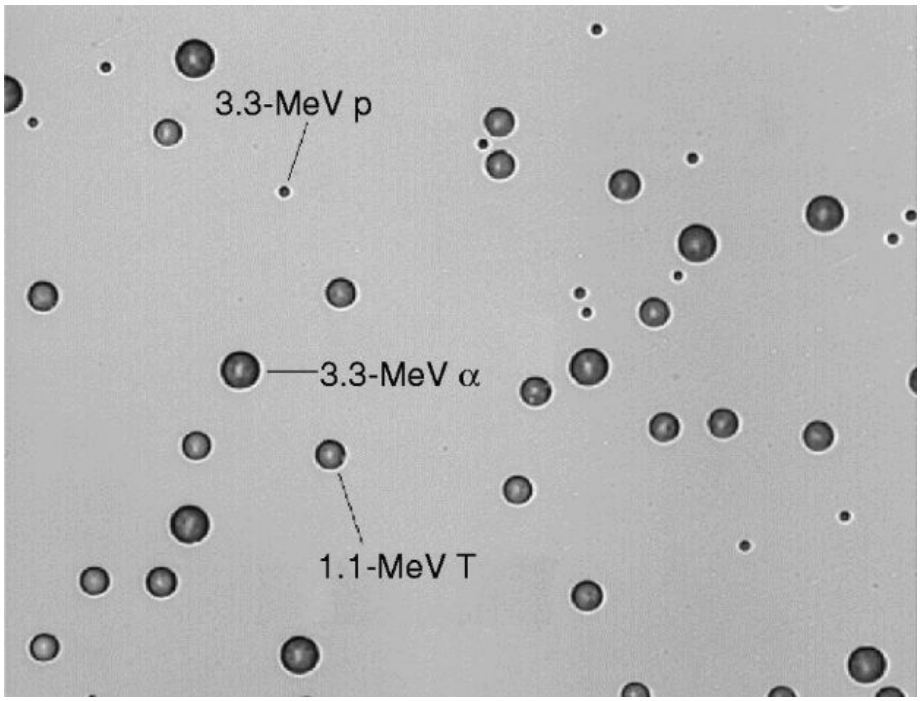

**Fig. 14.** Plasma particles related etched tracks to show SSNTD discriminating characteristics for fusion diagnostics.

It is a common view that deuteron plasma diagnostics are of increasing importance for future fusion (D-D) devices. In these machines several reactions are expected to take place and as it is shown in Table 9, most of them are involving neutrons.

**Table 9.** Fusion reactions involving neutrons expected in a plasma device.

| | |
|---|---|
| Primary | $D + D \rightarrow T^* (1.01\ MeV) + p^* (3.02\ MeV)$ |
| | $D + D \rightarrow n (2.45\ MeV) + {}^3He^* (0.82\ MeV)$ |
| | $D + T \rightarrow \alpha^* (3.5\ MeV) + n (14.1\ MeV)$ |
| | $T + T \rightarrow \alpha^* (\leq 6.6\ MeV) + 2\ n (\leq 10.6\ MeV)$ |
| | $D + {}^3He \rightarrow \alpha^* (3.6\ MeV) + p^* (14.7\ MeV)$ |
| | $T + {}^3He \rightarrow \alpha^* (4.8\ MeV) + D^* (9.5\ MeV)\ (\sim 43\%)$ |
| | $T + {}^3He \rightarrow \alpha + p + n + 12.1\ MeV\ (\sim 51\%)$ |
| | $T + {}^3He \rightarrow {}^5He (2.4\ MeV) + p (11.9\ MeV)\ (\sim 6\%)$ |
| Secondary[a] | ${}^3He (\leq 0.82\ MeV) + D \rightarrow \alpha (6.6 - 1.7\ MeV) + p^* (12.6 - 17.5\ MeV)$ |
| | $T (\leq 1.01\ MeV) + D \rightarrow \alpha (6.7 - 1.4\ MeV) + n (11.9 - 17.2\ MeV)$ |
| | $n (14.1\ MeV) + p \rightarrow n' + p^* (\leq 14.1\ MeV)$ |
| | $n (14.1\ MeV) + D \rightarrow n' + D^* (\leq 12.5\ MeV)$ |
| | $n (14.1\ MeV) + T \rightarrow n' + T^* (\leq 10.6\ MeV)$ |
| | $n (14.1\ MeV) + {}^3He \rightarrow n' + {}^3He^* (\leq 10.6\ MeV)$ |
| | $n (2.45\ MeV) + p \rightarrow n' + p^* (\leq 2.45\ MeV)$ |
| | $n (2.45\ MeV) + D \rightarrow n' + D (\leq 2.18\ MeV)$ |
| | $n (2.45\ MeV) + T \rightarrow n' + T (\leq 1.84\ MeV)$ |
| | $n (2.45\ MeV) + {}^3He \rightarrow n' + 3He (\leq 1.84\ MeV)$ |
| Tertiary[b] | $n (\leq 12.5\ MeV) + {}^3He \rightarrow \alpha + p (\leq 30.8\ MeV)$ |

Superindex *a* and *b* indicate that the reactions do not follow the given sequence and the asterisk is related to laser-plasma induced reaction. Plasma diagnostics, e.g. on reverse field experiment (RFX as part of the ITER project), employed NTM to provide the external neutron field values around the RFX-installation during pulsed operation. During this study latent tracks were etched in a solution of 6.25M KOH at 60 ºC [45]**.** Neutron density was measured around the toroidal machine as shown in Fig. 15, in that track size distribution is reported for the tested location.

From these histograms, it was deduced that the neutron intensity changes at most 40%, and in opposition to expected values the epithermal component is quite low (60%) since the neutron region below a few MeV was supposed to be negligible. Nevertheless, estimated neutron fluence for the whole experiment is 7.5 x $10^{10}$ +/-12% neutrons $cm^{-2}$. The uneven neutron field clearly evidenced by the track hystograms is related to the fact that the FRX-mod facility is dedicated mainly to plasma diagnostics; several equipment introduce uneven shielding and neutron scattering. At position 2 and 5, it is possible to observe that the neutron energy shifted in comparison to other locations; as it can be deduced from the existence of larger tracks where the converter alphas are observable. The explication is related to the induced fusion reaction ($D+D \rightarrow {}^3He+n$, Q-value 3.30 MeV) and 2.45 MeV is the neutron kinetic energy (0.8 MeV belongs to reaction fragment). As neutrons leave the vessel‘s inner volume, neutrons are expected to conserve their kinetic energy so as to induce mainly proton recoils in the PADC. This is observed in all locations excepting two of them (lcations 2 and 5), in this case, histograms end points are near 12 μm; on the other hand, track histogram extends above this value reaching almost twice as much; coincidentally in the region

where tracks related to $^{10}$B-converter alphas are expected. In Fig. 16, we reported the reaction cross section related to $^{10}$B(n,α) reaction in the region of interest.

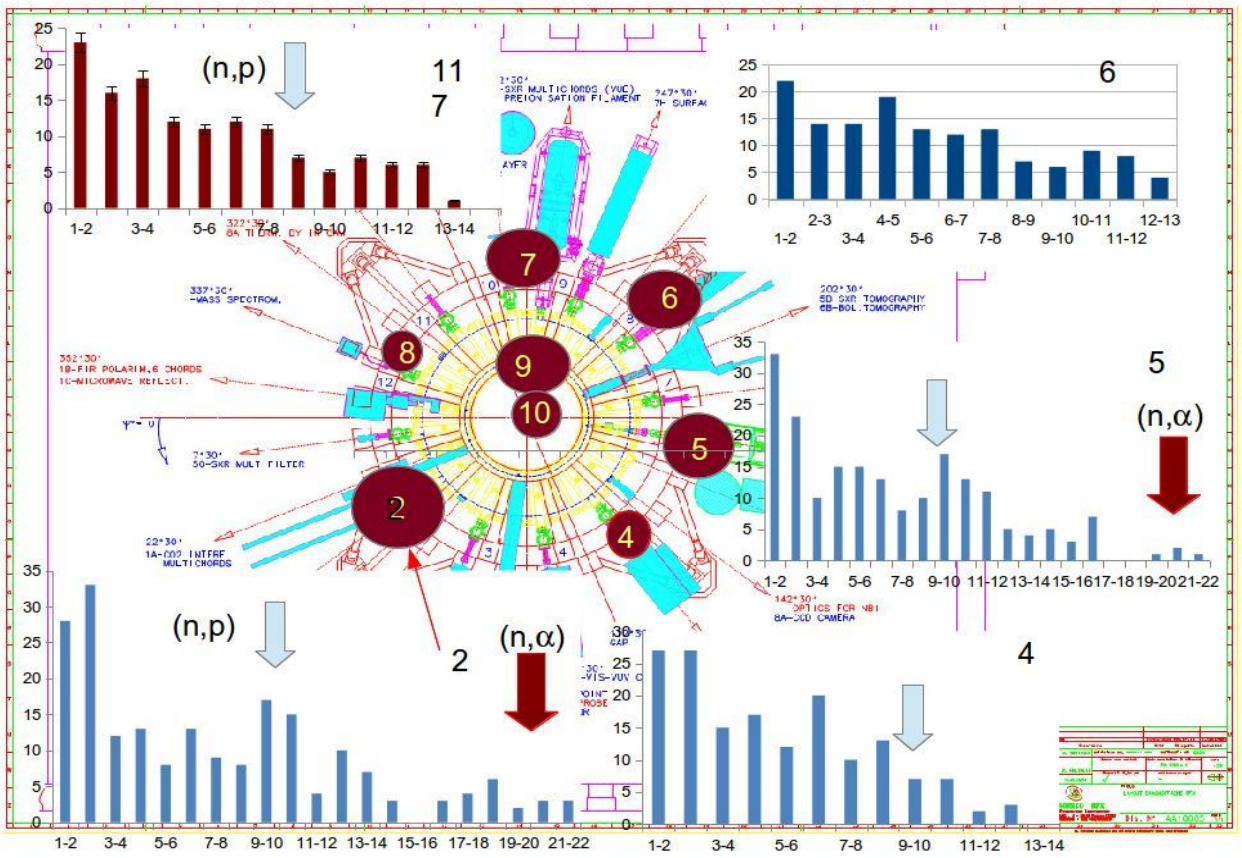


**Fig. 15.** Layout of the fusion RFX machine at Padua, Italy showing track histograms related to neutrons that escape from the vicinity of fusion containment vessel. Numbers and background size indicate neutron location and intensity. The abscissa values in the histograms are in micrometers.

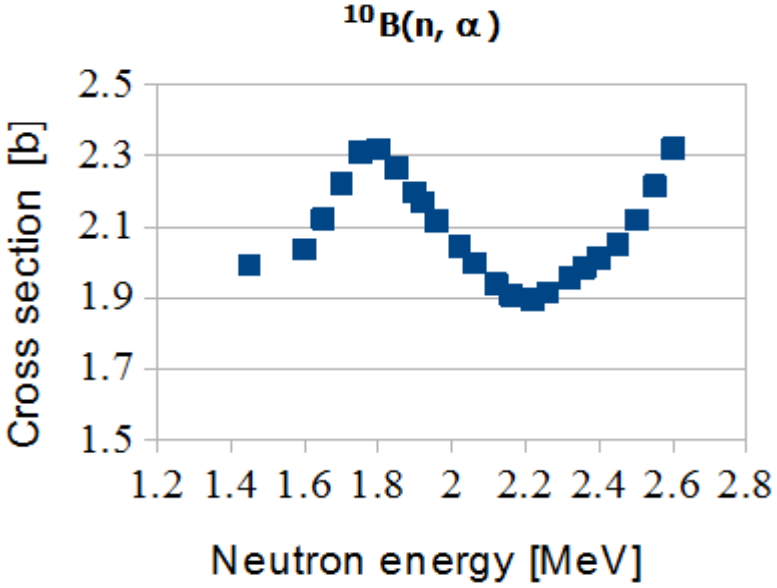


**Fig. 16.** Boron-10 reaction cross section for a small neutron energy region of interest.

As the neutron energy shifts, the (n,α) reaction cross section decreases and mainly proton recoils dominate the track distribution as can be seen for position 7 in Fig. 15. In the case the neutrons maintain the 2.45 MeV kinetic energy a larger number of alpha tracks would be present; we expect

an etched track size distribution as given in Fig. 17. Track or at least a peak superposes to recoils of protons and heavier particles.

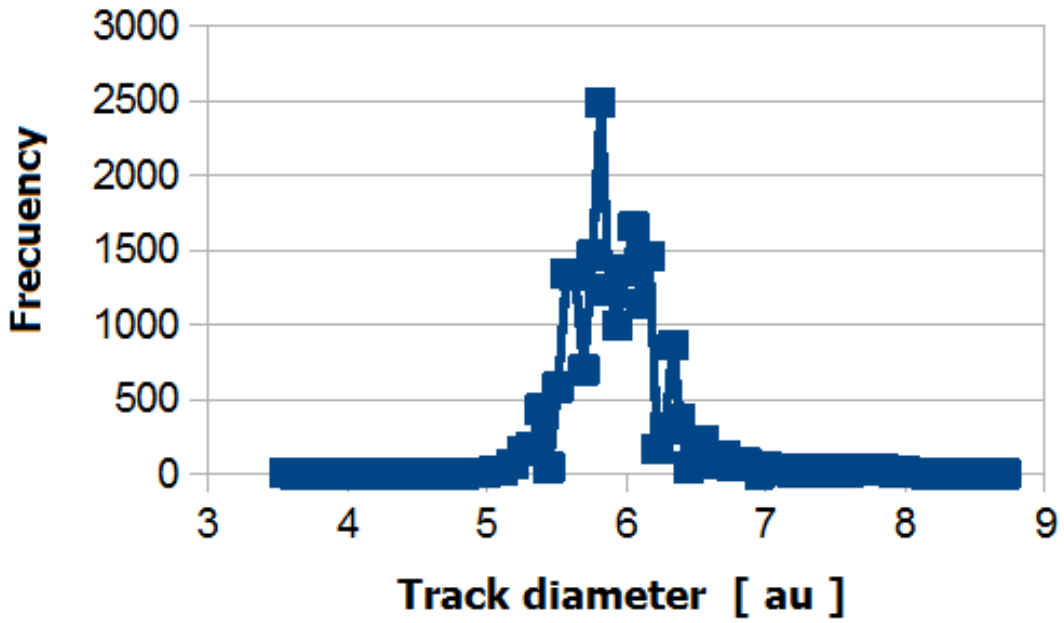


**Fig. 17.** Track distribution response to monoenergetic alpha source. Track diameter mean value of 16.13 μm, with a standard deviation = 0.81.

In Fig. 17, we report the average value of etched track diameter distribution, related to mono-energetic alpha source, of 16.13 μm with an error around 12% and FWHM of a remarkably low value of 5% to illustrate what should be observed on, e.g., for position No. 5 for larger track size.

Since the expected result is not observed we conclude that the original neutron energy group around 2.45 MeV+/- 234 keV (FWHM=9.5%) may be shifted by 10% to lower energies; possibly explained by shielding effect given by the equipment and the machine structural elements as can be discerned from Fig. 18 available on internet.

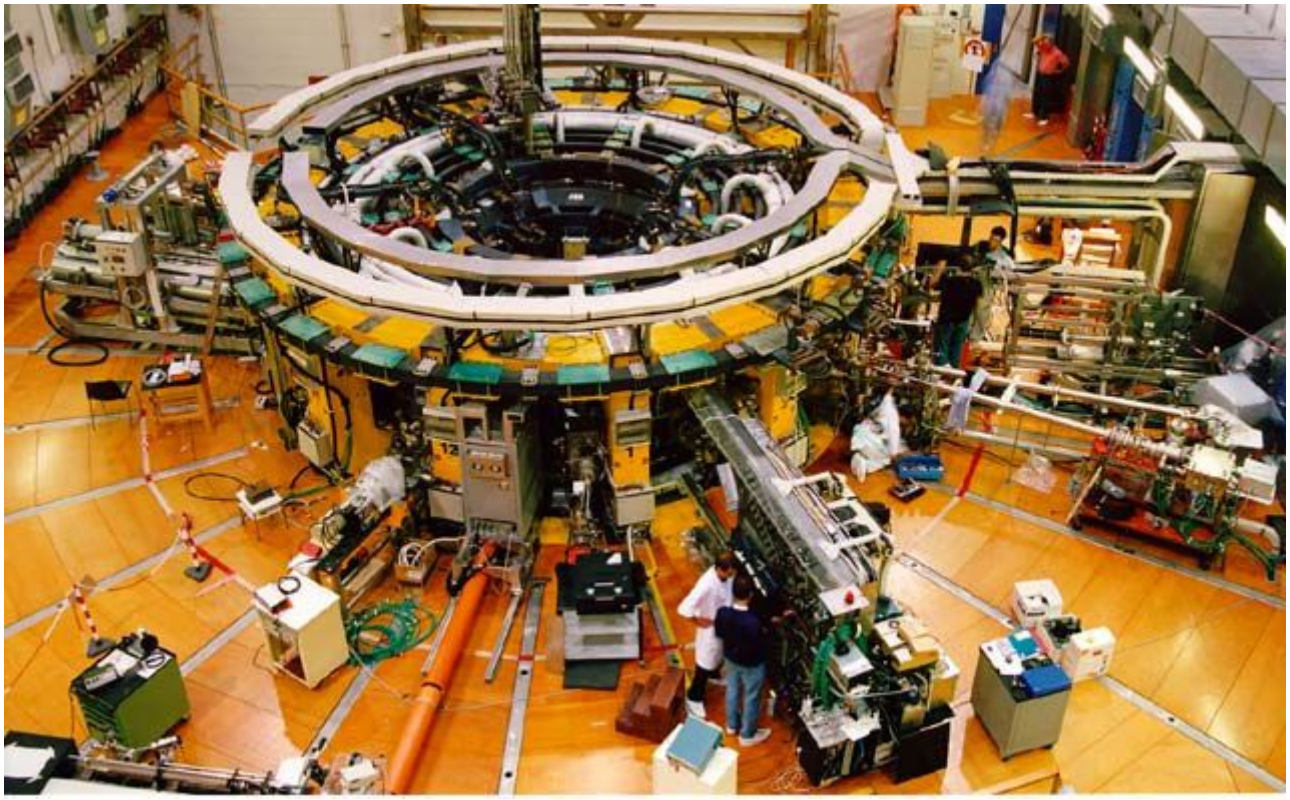

**Fig. 18.** Illustration of the FRX-Mod facility at CNR of Padua, Italy to show equipment and the machine structural elements.

## 8. Summary

SSNTD is a mature technology widely used to measure neutron fluences and doses by analysing the tracks induced by the radiation on a small piece of polymer. Materials like Lexan, Makrofol, LR-115, CR-39, etc. are used as track detectors. Once exposed to radiation, etching process is used for revelation of tracks in the track detectors. A sensible topic is the calibration procedure because the efficiency (or response) in track/neutron depends upon the neutron spectrum, and the etching procedure. When SSNTDs are used for dosimetry or to measure the total neutron fluence, the neutron spectrum of the source used for calibration must be alike the neutron spectrum to be measured. To increase the efficiency, materials are used as converters, or in combination with degraders. Neutron contamination in the radiotherapy facilities with Linac is a radiation protection issue, several efforts have been carried out to determine the neutron fluence, the dose and the neutron spectrum. During cancer treatment in the radiation hall a strong, pulsed and mixed radiation field is produced, therefore, measuring devices must be based upon a passive detector, as the SSNTD. From the available SSNTDs, we have reviewed the features of CR-39$^{TM}$ like the etching procedure, calibration conditions and obtained results to measure the photo-neutrons produced around radiotherapy Linacs and in fusion studies.

## References


[1] L. Sajo Bohus, Ma. M Mackowiak de Antczak, E. D. Greaves, A. Antczak, J. Bermudez, Zs. Kasztovszky, T. Poirier, A. Simonits, Incipient Archaeometry in Venezuela: Provenance study of Pre-hispanic pottery figurines, J. Radioanal. Nucl. Chem. 265 (2005) 247-256.

[2] H. Barros, L. Sajó-Bohus, Zs. Kasztovszky, H. Postma, P. Vermaercke, P. Schillebeeckx, D. Palacios, E.D. Greaves, M. Mackowiak de Antczak, Neutron methods for Amerindian

Archaeological Provenance study and authentication of Etruscan bronze art objects, Proc. 11th Intern. Conf. on Nuclear Reaction Mechanisms, Varenna, Villa Monastero-Italy, June 12 - 16, 2006.

[3] J.K. Pálfalvi, Y. Akatov, J. Szabó, L. Sajó-Bohus, I. Eördögh, Evaluation of solid state nuclear track detector stacks exposed on the International Space Station, Radiat. Prot. Dosim. 110 (2004) 784-788.

[4] R. Verma, M.V. Roshan, F. Malik, P. Lee, S. Lee, S.V. Springham, T.L. Tan, M. Krishnan, R.S. Rawat, Compact sub-kilojoule range fast miniature plasma focus as portable neutron source, Plasma Sources Sci. Technol. 17 (2008) 1-11.

[5] A. Malinowska, A. Szydlowski, M.J. Sadowski, J. Zebrowskia, M. Scholz, M. Paduch, M. Jaskola, A.Korman, Measurements of fusion produced protons by means of SSNTDs, Radiat. Meas. 43 (2008) S295-S298.

[6] Viesti G., Donzella A., Bonomi G., Botosso C., Fabris D., Lunardon M., Moretto S., Nebbia G., Pesente S., Pino F., Sajo-Bohus L., Zenoni A. Search of explosives in vehicles using tagged neutrons, NATO Science for Peace and Security B: Physics and Biophysics (2008) 39-46.

[7] Y. Yang, Y. Li, H. Wang, T. Li, B. Wu, Explosives detection using photoneutrons produced by X-rays, Nucl. Instrum. Meth. Phys. Res. A 579 (2007) 400–403.

[8] T. Gozani, D. Strellis, Advances in neutron based bulk explosive detection. Nucl. Inst. Meth. Phys. Res. B 261 (2007) 311-315.

[9] Y. Takahashi, T. Misawa, C.H. Pyeon, S. Shiroya, K. Yosikawa, Landmine detection method combined with backscattering neutrons and capture γ-rays from hydrogen, Appl. Radiat. Isot. 69 (2011) 1027-1032.

[10] IAEA, Combating illicit trafficking in nuclear and other radioactive material. International Atomic Energy Agency Nuclear Security Series No. 6, Vienna, 2007.

[11] I. Hee-Jung, S. Kyuseok, Applications of prompt gamma ray neutron activation analysis: Detection of illicit materials. Appl. Spect. Rev. 44 (2009) 317-334.

[12] IAEA, Combating illicit trafficking in nuclear and other radioactive material, International Atomic Energy Agency Nuclear Security Series No. 6. Vienna, 2007.

[13] F. Palacios, J. Ricardo, D. Palacios, L. Sajo-Bohus, 3-D Image reconstruction of nuclear tracks induced in CR-39 detectors by means of digital holography, AIP Conf. Procc. 884, (2007) 485-490.

[14] M. Markó, G. Krexner, J. Chefer, A. Szakái, L. Cser, Atomic resolution holography using advanced reconstruction techniques for two-dimensional detectors, New J. Phys. 12 (2010) 1-18.

[15] S.A. Martinez-Ovalle, R. Barquero, J.M. Gómez-Ros, A.M. Lallena, Neutron dose equivalent and neutron spectra in tissue for clinical linacs operating at 15, 18 and 20 MV. Radiat. Prot. Dosim. 147 (2011) 498-511.

[16] H.R. Vega-Carrillo, B. Hernández-Almaraz, V.M. Hernández-Dávila, A. Ortíz-Hernández, Neutron spectrum and doses in a 18 MV linac, J. Radioanal. Nucl. Chem. 283 (2010) 261-265.

[17] H.R. Vega-Carrillo, S.A. Martinez-Ovalle, A.M. Lallena, G.A. Mercado, J.L. Benites-Rengifo, Neutron and photon spectra in linacs, Appl. Radiat. Isot. 71 (2012) 75-80.

[18] IAEA, Radiological safety aspects of the operation of electron linear accelerator, International Atomic Energy Agency Technical Report Series 188, Vienna, 1979.

[19] M. Králik, K. Turek, Characterisation of neutron fields around high energy X-ray radiotherapy machines. Rad. Prot. Dosim. 110 (2004) 503-507.

[20] A. N. Ermakov, I. V. Makarenko, V. N. Orlin, Multi-particle photonuclear reactions behind Giant Dipole resonance, J. Korean Phy. Soc. 59 (2011) 1936-1939.

[21] N. Rozlosnik, L.Sajo-Bohus, C. Birattari, L. Biro, K. Havancsak, Direct observation of latent nuclear tracks in organic material by atomic force microscopy, Fourth Foresight Conf. on Molecular Nanotech. Nov. 5–9, 1997, Palo Alto, CA, USA.

[22] N. Rozlosnik, C.S. Glavak, J. Palfalvi, L. Sajo-Bohus, C. Birattari, E. Gadioli, Investigations of nuclear reaction products by Atomic Force Microscopy, Radiat. Meas. 28 (1997) 277–280.

[23] C. Vazquez-Lopez, R. Fragoso, J.I. Golzarri, F. Castillo-Mej, M. Fuji, G. Espinosa, The atomic force microscope as a fine tool for nuclear track studies, Radiat. Meas. 34 (2001) 189–191.

[24] R. Martín-Landrove, L. Sajo-Bohus, D. Palacios, Nuclear track evolution by capillary condensation during etching in SSNT detectors, Radiat. Meas. 50 (2013) 241-245.

[25] G. Somogyi, Development of etched nuclear tracks. Nucl. Instrum. Meth. 173 (1980) 21-42.

[26] D. Nikezic, D. Kostic, C. Yip, K.N. Yu, Comparison among different models of track growth and experimental data, Radiat. Meas. 41 (2006) 253-256.

[27] M. Fromm, A. Chambaudet, F. Membrey, Data bank for alpha particle tracks in CR39 with energies ranging from 0.5 to 5 MeV recording for various incident angles, Nucl. Tracks Rad. Meas. 15 (1998) 115-118.

[28] P.C. Kalsi, A. Ramaswami, V.K. Manchanda, Solid state nuclear track detectors and their applications, BARC Newsletter 257 (2005) 6-15.

[29] A.N. Garg, R.J. Batra, Isotopic sources in neutron activation analysis. J. Radioanal. Nucl. Chem. 98 (1986) 167-194.

[30] H.R. Vega-Carrillo, E. Manzanares-Acuña, M.P. Iñiguez, E. Gallego, A. Lorente, Spectrum of isotopic neutrons sources inside concrete wall spherical cavities. Radiat. Meas. 42 (2007) 1373-1379.

[31] D. Kiss, P. Quittner (Eds.), Neutron Physics, MTA, Budapest, Hungary. 1971.

[32] D. J. Hughes and C. Eggler, Cloud-chamber energy measurement of photo-neutron sources, Phys. Rev. 72 (1947) 902-906.

[33] N.E. Hertel, M.P. Shannon, Using the photoneutron interaction to detect special nuclear material, Procc. of the 38th Midyear Meeting of the Health Physics Society: Materials Control and Security: Risk Assessment, Handling, and Detection. New Orleans, Feb. 13-16, pp. 82-89: 2005.

[34] A. Chilton, J. Shultis, R. Faw, Principles of radiation shielding, Prentice-Hall, Englewood Cliffs, NJ, 1984.

[35] NCRP, Neutron contamination from medical electron accelerators, National Council on Radiation Protection and Measurements Report No. 79, Bethesda, MD, 1984.

[36] NCRP, Radiation protection for particle accelerator facilities, National Council on Radiation Protection and Measurements Report No. 144, Bethesda, MD, 2003.

[37] M. White, Development and implementation of photonuclear cross section data for mutually coupled neutron-photon transport calculations in MCNP. LA-13744-T Los Alamos National Laboratory, 2000.

[38] G. Foldiak, Industrial application of radioisotopes, MTA – Budapest, Hungary 1972.

[39] L. Sajó-Bohus, H. Barros, E.D. Greaves, H.R. Vega-Carrillo, Graphite moderated $^{252}$Cf source. Appl. Radiat. Isot., doi:10.1016/j.apradiso.2015.02.025, 2015.

[40] L. Sajo-Bohus, E.D. Greaves, J.K. Pálfalvi, Studies in interdisciplinary fields employing Nuclear track detectors (NTDs), in: N. Singh (Ed.) Radioisotopes – Applications in Bio-Medical Science, InTech, 2011, pp.173-196.

[41] L. Sajó-Bohus, J. K. Pálfalvi, O. Arevalo, E. D. Greaves, P. Németh, D. Palacios, J. Szabo, I. Eördögh, Neutron induced complex reaction analysis with 3D nuclear track simulation, Radiat. Meas. 40 (2005) 442-447.

[42] D.Nikezic, K. N.Yu, Three-dimensional Analytical Determination of the track parameters: Over-etched Tracks, Rad. Meas. 37 (2003) 39-45.

[43] J. Palfalvi, L. Sajo-Bohus, I. Eordogh, First international intercomparison of image analyzers, Radiat. Meas. 31 (1999) 157-166.

[44] J. Palfalvi, I. Eordog, K. Szasz, L. Sajo Bohus, A New Generation Image Analyzer for Evaluation SSNT Detector, Radiat. Meas. 28, (1997) 849-852.

[45] W. Gonzalez, G. Espinosa, M. Zuin, G. Viesti, F. Pino, J.I. Golzarri, E. Martines, J. Bermudez, D. Moro, J.K.Palfalvi, L. Sajo-Bohus, PADC detected external neutron field by nuclear tracks at RFX-mod, J. Nucl. Phys. Mat. Sci. Radiat. Appl. 2 (2014) 83–90.

[46] R. Barquero, R. Mendez, H.R. Vega-Carrillo, M.P. Iñiguez, T.M. Edwards, Neutron spectra and dosimetric features around an 18 MV Linac accelerator, Health Phys. 88 (2005) 48-58.

[47] R. Takam, E. Bezak, L.G. Marcu, E. Yeoh, Out-of-field neutron and leakage photon exposures and the associated risk of second cancers in high-energy photon radiotherapy: Current statuts, Radiat. Res. 176 (2011) 508-520.

[48] E. Bezak, R. Takam, L.G. Marcu, Peripheral photon and neutron doses from prostate cancer external beam irradiation, Radiat. Prot. Dosim. doi:10.1093/rpd/ncu362. 2015.

[49] R.A. Halg, J. Besserer, M. Boschung, S. Mayer, A.J. Lomax, U. Schneider, Measurements of the neutron dose equivalent for various radiation quantities, treatment machines and delivery techniques in radiation therapy, Phys. Med. Biol. 59 (2014) 2457-2468.

[50] A. Szydlowski, M. Jaskola, A. Malinowska, S. Pszona, A. Wysocka-Rabin, A. Korman, K. Pytel, R. Prokopowicz, J. Rostkowska, W. Bulski, M. Kuk, Application of nuclear track detectors as sensors for photoneutrons generated by medical accelerators, Radiat. Meas. 50 (2013) 74-77.

[51] V. L. Chakhlov, Z. W. Bell, M. M. Shtein, V. M. Golovkov, Photoneutron source based on a compact 10 MeV betatron, Nucl. Instr. Meth. Phys. Res. A 422 (1999) 5-9.

[52] M. Tatari, A.H. Ranjbar, Design of a photoneutron source based on 10 MeV electrons of radiotherapy linac, Ann. Nucl. Ener. 63 (2014) 69–74.

[53] A. Sari, M. Agelou, I. Bessieres, F. Carrel, M. Gmar, F. Laine, A. Lyoussi, S. Normand, A. Ostrowsky, L. Sommier, Characterization of the photoneutron flux emitted by an electron accelerator using an activation detector, IEEE Trans. Nucl. Sci. 60 (2013) 693-700.

[54] M.A. Saeed, Systematic treatment of photo-nuclear cross section calculations. J. Al Nahrain University-Science 11 (2008) 66-75.

[55] IAEA, Handbook on photonuclear data for applications. Cross-sections and spectra. IAEA-TECDOC-1178, International Atomic Energy Agency, Vienna, 2000.

[56] G. Tosi, A. Torresin, S. Agosteo, A. Folgio Para, V. Sangiust, L. Zeni, M. Silari, Neutron measurements around medical electron accelerators by active and passive detection techniques, Med. Phys. 18 (1991) 54-60.

[57] J.L. Benites-Rengifo, H.R. Vega-Carrillo, Photoneutron spectrum measured with Bonner sphere spectrometer in Planetario method mode, Appl. Radiat. Isot. 83 (2014) 256-259.

[58] J. C. Liu, K. R. Kase, X. S. Mao, W. R. Nelson, J. H. Kleck, S. Johnson, Calculations of photoneutrons from Varian Clinac accelerators and their transmissions in materials, SLAC-PUB-7404 Stanford Linear Accelerator Center, Stanford, CA. 1997.

[59] B.J. Patil, S.T. Chavan, S.N. Pethe, R. Krishnan, V.N. Bhoraskar, S.D. Dhole, Estimation of neutron production from accelerator head assembly of 15 MV medical LINAC using FLUKA simulations, Nucl. Instr. Meth. Phys. Res. B 269 (2011) 3261–3265.

[60] H.R. Vega-Carrillo, B. Hernandez-Almaraz, V.M. Hernandez-Davila, A. Ortiz-Hernandez, Neutron spectrum and dose in a 18 MV linac, J. Radioanal. Nucl. Chem. 283 (2010). 261-265.

[61] H.R. Vega-Carrillo, A. Ortiz-Hernandez, V.M. Hernandez-Davila, B. Hernandez-Almaraz, T. Rivera, H*(10) and neutron spectra around linacs, J. Radioanal. Nucl. Chem. 283 (2011) 537-540.

[62] J. Palfalvi, A.M. Bhagwat, L. Medveczky, Investigations on the Neutron Sensitivity of Kodak-Pathe LR 115 Recoil Track Detector, Health Phys. 41(3) (1981) 505-512.

[63] E. Savvidis, D. Sampsonidis, M. Zamani, A CR-39 Fast neutron dosemeter based on an (n,α) converter, Radiat. Prot. Dosim. 44(1-4) (1992) 341-342.

[64] M. Izerrouken, J. Skvarc, R. Ilic, A wide energy range personnel neutron dosimeter, Radiat. Meas. 37 (2003) 21– 24.

[65] R. Alvarado, D. Palacios, L. Sajo-Bohus, E.D. Greaves, I. Goncalves H. Barros, P. Nemeth, Neutron flux characterization using LR-115 NTD and binary glass metal as converter, Rev. Mex. Fís. S 56 (2010) 5-8.

[66] A.R. El-Sersy, N.E. Khaled, S.A. Eman, Determination of CR-39 detection efficiency for fast neutron registration and the absolute neutron dosimetry, Nucl. Instrum. Meth. Phys. Res. B 215 (2004) 443–448.

[67] A.Y. Hassen, N.F. Khadhm, Evaluation of the uranium concentrations in human tissues samples by fission fragments induced using CR-39 nuclear track detector, Int. J. Appl. Innov. Eng. Manag. 3 (2014) 98-104.

[68] J.K. Pálfalvi, J. Szabó, Yu. Akatov, L. Sajó-Bohus, I. Eördögh, Cosmic ray studies on the ISS using SSNTD, BRADOS Projects, 2001-2003, Radiat. Meas. 40 (2005) 428-432.

[69] J. Szabó, J.K. Pálfalvi, V.A. Shurshakov, R.V. Tolochek, Preliminary results of the SPD Box Experiments onboard ISS, 16th Workshop on Radiation Monitoring for the International Space Station, 6-8 September 2011.

[70] V. Kumar, R.G. Sonkawade, A.S. Dhaliwal, Optimization of CR-39 as neutron dosimeter, Indian J. Pure Appl. Phys. 48 (2010) 466-469.

[71] Matiullah, K. Kudo, X. Yang, Calibration of Various Types of Neutron Dosimeters in a Heavy Water Moderated and Monoenergetic Neutron Fields-II. Experimental, Radiat. Meas. 22 (199) 687-690.

[72] IAEA, Compendium of neutron spectra and detector responses for radiation protection purposes.Technical reports series No. 318, International Atomic Energy Agency, Vienna, 1990.

[73] C. Brun, M. Fromm, M. Jouffroy, P. Meyer, J.E. Groetz, F. Abel, A. Chambaudet, B. Dorschel, D. Hermsdorf, R. Bretschneider, K. Kadner, H. Kuhne, Intercomparative study of the detection characteristics of the CR-39 SSNTD for Light Ions: Present status of the Besancon-Dresden approaches, Radiat. Meas. 31 (1999) 89-98.

[74] J. K. Pálfalvi, L. Sajó-Bohus, J. Szabó, J. Pálfalvi Jr., Study on etching of PADC track etch detector by an alpha source, Under Preparation (2015).

[75] J.K. Pálfalvi, L. Sajo-Bohus, M. Balasko, I. Balashzy, Neutron field mapping and dosimetry by CR-39 for radiography and other applications, Radiat. Meas. 34 (2001) 471-475.

[76] N. Bohr, J.A. Wheeler, The mechanism of nuclear fission, Phys. Rev. 56 (1939) 426-42.

[77] G. Bernardini, R. Reitz, E. Segre, Photo-mesonic fission of bismuth, Phys. Rev. 90 (1953) 573-574.

[78] J. Goldemberg, L. Katz, Photoneutron cross sections of some elements, Canadian J. Phys. 32 (1954) 49-59.

[79] P.A. Dickey and P. Axel, U-238 and Th-232 Photo-fission and photo-neutron emission near threshold, Phys. Rev. Lett. 35 (1975) 501-504.

[80] D. I. Thwaites, J. B. Tuohy, Back to the future: the history and development of the clinical linear accelerator, Phys. Med. Biol. 51 (2006) R343–R362.

[81] X.G. Xu, B. Bednarz, H. Paganetti, A review of dosimetry studies on external-beam radiation treatment with respect to second cancer induction, Phys. Med. Biol. 53 (2008) R193-R241.

[82] A. Naseri, A. Mesbahi, A review on photoneutrons characteristics in radiation therapy with high-energy photon beams, Rep. Pract. Oncol. Radiother. 15 (2010) 138-44.

[83] S.M. Hashemi, B. Hashemi-Malayeri, G. Raisali, P. Shokrani, A.A. Sharafi, A study of the photoneutron dose equivalent resulting from a Saturn 20 medical linac using Monte Carlo method. Nukleonika 52 (2007) 39-43.

[84] K. Polaczek-Grelik, A. Orlef, M. Dybek, A. Konefal, W. Zipper, Linear accelerator therapeutic dose-induced radioactivity dependence, Appl. Radiat. Isot. 68 (2010) 763-766.

[85] H.R. Vega-Carrillo, S.A. Martínez-Ovalle, A.M. Lallena, G.A. Mercado, J.L. Benites-Rengifo, Neutron and photon spectra in Linacs, Appl. Rad. Isot. 71 (2012) 75-80.

[86] L. Jao-Perng, Ch. Tieh-Chi, L. Sung-Yen, L. Mu-Tai, The measurement of photoneutrons in the vicinity of a Siemens Primus linear accelerator, Appl. Radiat. Isot. 55 (2001) 315–321.

[87] P.H. McGlinley, M. Wood, M.Mills, R. Rodriguez. Dose levels due to neutrons in the vicinity of high-energy medical accelerators, Med. Phys. 3 (1976) 397-402.

[88] NCRP, Neutron contamination from medical electron accelerators. Report No. 79 National Council on Radiation Protection and Measurements, Bethesda, MD, 1989.

[89] R. Martín-Landrove, L. Sajo-Bohus, L. Spencer, D. Palacios, J. Dávila, Contribution of (n,γ) Reaction in the Out-of-Field Absorbed Dose for Patients under Radiotherapy Treatments with High MV Linear Accelerators, presented at the X Latin American Symposium on Nuclear Physics and Applications (X LASNPA), December 1-6 2013 Montevideo, Uruguay.

[90] MedicalDealer. [on line]. Market Analysis: Radiation oncology. <http://medicaldealer.com/market-analysis-radiation-oncology/>. [Reviewed on May 2015].

[91] H.R. Vega-Carrillo, R. Barquero, G.A. Mercado, Passive neutron area monitor with CR39, Int. J. Radiat. Res. 11 (2013) 149-153.

[92] R. Bedogni, A. Esposito, A. Gentile, M. Angelone, G. Gualdrini, Determination and validation of a response matrix for a passive Bonner sphere spectrometer based on gold foils, Radiat. Meas. 43 (2008) 1104-1107.

[93] R. Bedogni, P. Ferrari, G. Gualdrini, A. Esposito, Design and experimental validation of a Bonner sphere spectrometer based on Dysprosium activation foils, Radiat. Meas. 45 (2010) 1201-1204.

[94] S. Mayer, M. Boschung, Comparison of different PADC materials for neutron dosimetry, Radiat. Prot. Dosim. 161 (2014) 104-107.

[95] C. L. Lee, X.L. Zhou, R. J. Kudchadker, F. Harmon, Y. D. Harker, A Monte Carlo dosimetry-based evaluation of the $^{7}Li(p,n)^{7}Be$ reaction near threshold for accelerator boron neutron capture therapy, Med. Phys. 27(1) (2000) 192-202 .

[96] Ke Guotua, Sun Ziyonga, Shen Fenga, Liu Tiancaia, Li Yiguoa,, Zhou Yongmao, The study of physics and thermal characteristics for in-hospital neutron irradiator (IHNI), App. Radiat. Isot. 67 (2009) S234–S237.

[97] C.L. Tessa, T. Berger, R. Kaderka, D. Schardt, S. Burmeister, J. Labrenz, G. Reitz, M. Durante, Characterization of the secondary neutron field produced during treatment of an anthropomorphic phantom with x-rays, protons and carbon ions, Phys Med Biol. 59 (2014) 2111-2115.

[98] R.M. Howell, S. F. Kry, E. Burgett, N. E. Hertel, D. S. Followill, Secondary neutron spectra from modern Varian, Siemens, and Elekta linacs with multileaf collimators, Med. Phys. 36 (2009) 4027-4038.

[99] Matiullah, K. Kudo, X Yanh, Calibration of various types of neutron dosimeters in a Heavy water moderated and monoenergetic neutron fields-II. Experimental, Nucl. Radiat. Meas. 22 (1991) 687-690.

[100] F. H. Séguin, J. A. Frenje, C. K. Li, D. G. Hicks, S. Kurebayashi, J. R. Rygg, B.-E. Schwartz, R. D. Petrasso, Spectrometry of charged particles from inertial-confinement-fusion plasmas, Rev. Scien. Instr. 74 (2003) 975-995.

[101] W. Dunn, J.K. Shultis, Exploring Monte Carlo methods. Elsevier, Holland, 2012.

[102] M. Kralik, A. Aroua, M. Grecescu, V. Mares, T. Novotny, H. Schraube, B. Wiegel, Specification of Bonner sphere system for neutron spectrometry, Radiat. Prot. Dosim. 70 (1997) 279-284.

[103] H.R. Vega-Carrillo, B.W. Wehring, K.G. Veinot, N.E. Hertel, Response matrix for a multisphere spectrometer using a $^{6}LiF$ thermoluminescent dosimeter. Radiat. Prot. Dosim. 81 (1999) 133-140.

[104] H.R. Vega-Carrillo, E. Manzanares-Acuña, V.M. Hernadez-Davila, G.A. Mercado Sanchez, Response matrix of a multisphere neutron spectrometer with an $^{3}He$ proportional counter, Rev. Mex. Fis. 51 (2005) 47-52.

[105] R. Bedogni, A. Esposito, A. Gentile, M. Angelone, G. Gualdrini, Determination and validation of a response matrix for a passive Bonner sphere spectrometer based on gold foils. Radiat. Meas. 43 (2008) 1104-1107.

[106] H.R. Vega-Carrillo, E. Gallego, A. Lorente, Response matrix of a BSS/$^{6}LiI(Eu)$. Nucl. Tech. 168 (2009) 359-362.

[107] J.S. Wan, G.N. Zhu, Y. Zhao, N.N. Liu, Q.C. Zhuang, L.X. Zhang, Sh.L. Guo, Computer studies of detection efficiency of fast neturon spectrum based on PADC using the Monte Carlo method, Radiat. Meas. 36 (2003) 163-197.

[108] J.F Briestmeister (ed), MCNP$^{TM}$ - A general Monte Carlo N-particle transport code, Version4C, Report LA-13709-M Los Alamos National Laboratory, 2000.

[109] J.F. Ziegler, J.P. Biersack, U. Littmark, The stopping and range of ions in solids, Pergamon Press, New York, 1985.

[110] H. Zaki-Dizaji, M. Shahriari, G.R. Etaati, Monte Carlo calculation of CR-39 efficiency for fast neutron detection using a combination of MCNP and SRIM codes, and comparison with experimental results, Radiat. Meas. 42 (2007) 1332-1334.

[111] A.A.M. Aslam, K. James, S.A. Durrani, A computer program for the development of a fast neutron spectrometer based on electrochemically etched CR-39 detectors with radiator and degraders, Nucl. Track Radiat. Meas. 13 (1987) 131-137.

[112] A.A.M. Aslam, S.A. Durrani, Fast neutron spectrometry based on the registration of proton recoils in electrochemically etched CR-39 detector: Part II Theoretical, Nucl. Track Radiat. Meas. 15 (1988) 503-506.

[113] G. Dajko, Fast neutron spectrometry using CR-39 track detectors. Radiat. Prot. Dosim. 34 (1990) 9-12.

[114] G. Saint Martin, F. López, O.A. Bernaola, Neutron dosimetry device using PADC nuclear track detectors, J. Radioanal. Nucl. Chem. 287 (2011) 635-638.

[115] R. Barquero, R. Mendez, H.R. Vega-Carrillo, M.P. Iñiguez, T.M. Edwards, Neutron spectra and dosimetric features around an 18 MV linac accelerator, Health Phys. 88 (2005) 48-58.

[116] MCNPX, Monte Carlo N-particle transport code system for multiparticle and high-energy applications. Version 2.3.0, Report LA-UR-02-2607 Los Alamos National Laboratory, 2002.